Topological invariants for interacting topological insulators. I. Efficient numerical evaluation scheme and implementations

Yuan-Yao He,[1] Han-Qing Wu,[1] Zi Yang Meng,[2] and Zhong-Yi Lu[1]
[1]*Department of Physics, Renmin University of China, Beijing 100872, China*
[2]*Beijing National Laboratory for Condensed Matter Physics, and Institute of Physics, Chinese Academy of Sciences, Beijing 100190, China*
(Received 22 December 2015; revised manuscript received 29 March 2016; published 31 May 2016)

The aim of this series of two papers is to discuss topological invariants for interacting topological insulators (TIs). In the first paper (I), we provide a paradigm of efficient numerical evaluation scheme for topological invariants, in which we demystify the procedures and techniques employed in calculating Z_2 invariant and spin Chern number via zero-frequency single-particle Green's function in quantum Monte Carlo (QMC) simulations. Here we introduce an interpolation process to overcome the ubiquitous finite-size effect, so that the calculated spin Chern number shows ideally quantized values. We also show that making use of symmetry properties of the underlying systems can greatly reduce the computational effort. To demonstrate the effectiveness of our numerical evaluation scheme, especially the interpolation process, for calculating topological invariants, we apply it on two independent two-dimensional models of interacting topological insulators. In the subsequent paper (II), we apply the scheme developed here to wider classes of models of interacting topological insulators, for which certain limitation of constructing topological invariant via single-particle Green's functions will be presented.

DOI: 10.1103/PhysRevB.93.195163

I. INTRODUCTION

Topological insulators (TIs) [1,2] in free fermion systems can be characterized by topological invariants, such as Z_2 invariant and spin Chern number, and the calculation of these topological invariants is straightforward via noninteracting Hamiltonian matrix. However, the characterization of interacting topological insulators via these topological invariants is still not well understood, both conceptually and technically in numerical calculation. Of course, there are already various achievements. In the quantum (anomalous) Hall insulators [3,4] with broken time-reversal symmetry, the characterizing topological invariant is the Thouless-Kohmoto-Nightingale-den Nijs (TKNN) invariant [5,6], or first Chern number, which takes integer values. For TIs protected by time-reversal symmetry and charge $U(1)$ symmetry, the Z_2 topological index is applied to describe the system [7–9]. With additional $U(1)$ spin rotational symmetry in TIs, the $U(1)_{\text{spin}} \times U(1)_{\text{charge}} \rtimes Z_2^T$ symmetry (Z_2^T stands for time-reversal symmetry) results in $\mathbb{Z}$ classification and the appropriate topological invariant is the spin Chern number C_s [10,11], which is actually the case for the Kane-Mele model without Rashba spin-orbit coupling [7,8]. In such systems, the spin Hall conductivity $\sigma_{xy}^{\text{spin}}$ is related to spin Chern number as $\sigma_{xy}^{\text{spin}} = C_s \frac{e}{2\pi}$.

For noninteracting TIs, both Z_2 invariant [8,9] and spin Chern number [10,11] can be simply evaluated from the Hamiltonian matrix in band basis. For example, if a system has spatial inversion symmetry, the Z_2 invariant can be calculated as a product of parity eigenvalues of all occupied energy bands at all time-reversal invariant momentum (TRIM) points in the Brillouin zone (BZ) [12]. Spin Chern number, on the other hand, can be calculated by simply integrating Berry curvature over the BZ.

For interacting TIs, the evaluation of topological invariants becomes much more difficult and subtle. The proposals include constructing topological invariants from single-particle Green's function [6,13–18] or imposing twisted boundary phases to the ground state wave function [19,20]. Recently, the constructions of topological invariants from single-particle Green's function, especially the zero-frequency version [21,22], have been actively investigated. Implementations of topological invariants constructed from zero-frequency single-particle Green's function [21] in many-body numerical techniques have been carried out in various studies. In the one-dimensional Su-Schrieffer-Heeger model [23], the winding number based on zero-frequency single-particle Green's function is calculated by DMRG method in distinguishing topologically nontrivial and trivial phases. By LDA+Gutzwiller and LDA+DMFT methods, the Z_2 invariant has been applied in identifying the correlated TIs SmB_6 [24] and PuB_6 [25]. The Z_2 invariant has also been calculated in QMC [26–29] and cluster perturbation theory [30,31] for various generalizations of the Kane-Mele-Hubbard model. Moreover, there are dynamical mean-field theory calculations of the Bernevig-Hughes-Zhang model with interactions in which the Z_2 invariant is calculated [32–34]. As for spin Chern number constructed from zero-frequency single-particle Green's function, it has been applied to verify the topological phase transitions in the Kane-Mele-Hubbard model by quantum Monte Carlo [28,29] and cellular dynamical mean-field theory (CDMFT) [35].

The issue of evaluating spin Chern number for interacting topological insulators in CDMFT [35], or more generally quantum cluster methods [36], is that the correlation effects can only be captured inside the small cluster, even through the calculated spin Chern number is quantized due to the mean-field bath at the thermodynamic limit. Nevertheless, such approaches cannot faithfully monitor the topological phase transitions with a length scale larger than the cluster size involved. On the other hand, QMC is more accurate in capturing both short- and long-range correlation effects by handling supercell with much larger size, but, in obtaining topological invariants, it suffers from finite-size effect and the topological invariants calculated from QMC for interacting

 ©2016 American Physical Society

TIs are not exactly integer quantized [26,28]. Actually, due to finite size effect, spin Chern number can be even far away from expected integer results [28]. Thus, it will be a great improvement if one can bring the merit of CDMFT (its thermodynamic limit) into QMC to overcome the finite-size effect in topological invariants, since the integer quantization of topological invariants is essential for achieving well-defined topological phases and identifying topological phase transitions. Here, we provide such a scheme.

In this paper, employing large-scale quantum Monte Carlo simulations for interacting TIs, we eliminate the severe finite-size effect and obtain quantized topological invariants by introducing an interpolation process and imposing symmetries of the studied systems. The numerical evaluation scheme of both Z_2 invariant and spin Chern number constructed from zero-frequency single-particle Green's function proposed in Ref. [21] is systematically presented with all important details. To demonstrate the strength of our calculation scheme, especially the interpolation process, we test it on two independent 2D models of interacting TIs, in which the topological phase transitions driven by one-body model parameters are detected by the integer-quantized topological invariants.

The rest of the paper is organized as follows. In Sec. II, despite the already existing literature [16,17,20,21,37–39], the construction of the Z_2 invariants and spin Chern number via zero-frequency single-particle Green's function is discussed for the sake of a self-contained narrative. A brief introduction of projector quantum Monte Carlo method is also presented. Then our numerical calculation scheme and the interpolation technique for these topological invariants are introduced in detail in Sec. III. After that, we show the applications of our scheme in Sec. IV, based on QMC simulations for two independent 2D model systems of interacting TIs. Finally, Sec. V summarizes our method and makes connection with the paper (II) in this series on identifying interaction-driven topological phase transitions without symmetry breaking by the topological invariants calculated via the scheme presented here for interacting topological insulators, where the limitation of topological invariants constructed from the single-particle Green's function is clearly manifested.

II. TOPOLOGICAL INVARIANTS AND QUANTUM MONTE CARLO METHOD

A. Z_2 invariant and spin Chern number

In interacting fermion systems, the single-particle Green's function is given as $G(i\omega,\mathbf{k}) = [i\omega + \mu - \mathcal{H}(\mathbf{k}) - \Sigma(i\omega,\mathbf{k})]^{-1}$, where $\Sigma(i\omega,\mathbf{k})$ is the self-energy originating from interaction. The zero-frequency single-particle Green's function is Hermitian [21], and we can obtain its real eigenvalues by diagonalizing the Green's function matrix $G(i\omega = 0,\mathbf{k})_{N_O\times N_O}$, where N_O is the number of orbitals or bands. In the language of Ref. [22], the topological invariants can be defined as follows. We simply define the so-called topological Hamiltonian $h_t(\mathbf{k}) = -G^{-1}(i\omega = 0,\mathbf{k})_{N_O\times N_O}$, and then calculate the topological invariant as if $h_t(\mathbf{k})$ is a noninteracting Bloch Hamiltonian. The advantage of $h_t(\mathbf{k})$ is that it reduces to the free Bloch Hamiltonian in the noninteracting limit. Equivalently, we can work with $G(i\omega = 0,\mathbf{k})_{N_O\times N_O}$, since the eigenvectors of $G(i\omega = 0,\mathbf{k})_{N_O\times N_O}$ and $-G^{-1}(i\omega = 0,\mathbf{k})_{N_O\times N_O}$ are the same.

In this paper we study systems with both time-reversal symmetry and $U(1)$ spin-rotational symmetry, indicating S_z conservation. Taking the $U(1)$ spin rotational symmetry into account, we can see that the Green's function is diagonal with respect to the spin index, and the two submatrices are denoted as G_σ ($\sigma = \uparrow, \downarrow$), each of which can be diagonalized as $G_\sigma(0,\mathbf{k})|\phi_m(0,\mathbf{k})\rangle = \mu_m(0,\mathbf{k})|\phi_m(0,\mathbf{k})\rangle$. Both Z_2 invariant and spin Chern number can be simply constructed from the eigenvectors $|\phi_m(0,\mathbf{k})\rangle$. For time-reversal invariant and spatial-inversion-symmetric systems with interactions, the Z_2 invariant can be constructed from $|\phi_m(0,\mathbf{k})\rangle$ at TRIM points. The Z_2 invariant can be expressed as [21]

$$(-1)^\nu = \prod_{\boldsymbol{\kappa}\in \mathrm{TRIM}} \prod_{\mu_m>0} \eta_m(\boldsymbol{\kappa}), \tag{1}$$

with $\eta_m(\boldsymbol{\kappa}) = \langle\phi_m(0,\boldsymbol{\kappa})|\hat{P}|\phi_m(0,\boldsymbol{\kappa})\rangle$,$\boldsymbol{\kappa}$ stands for TRIM points. and $\hat{P}$ is the spatial inversion symmetry operator. Here we have already taken the Kramer's degeneracy at TRIM points into consideration, and we only incorporate the parity in one spin sector in Eq. (1). This expression of Z_2 invariant is a generalization of that for the free fermion system to interacting systems. Note that $\{|\phi_m\rangle\}$ ($\mu_m > 0$) reduces to the filled Bloch bands in the noninteracting limit. Numerical evaluation of this Z_2 invariant in correlated systems is quite simple, and it has been demonstrated [26–29,33,35] that this topological invariant works well in detecting topological phase transition with a change of Z_2 invariant in weakly correlated systems.

So far we only discussed the Z_2 invariant. Due to the $U(1)$ spin-rotational symmetry, there is actually a Z invariant, which contains more information. To introduce this Z invariant, let us recall the TKNN or Chern number of fermion systems with broken time-reversal symmetry, which has been generalized to interacting fermion systems as [21]

$$\mathcal{C} = \frac{1}{2\pi}\iint_{\mathbf{k}\in BZ} d^2\mathbf{k}\mathcal{F}_{xy}(\mathbf{k}) \tag{2}$$

with

$$\begin{aligned}\mathcal{F}_{xy}(\mathbf{k}) &= \partial_{k_x}\mathcal{A}_y(\mathbf{k}) - \partial_{k_y}\mathcal{A}_x(\mathbf{k})\\ \mathcal{A}_i(\mathbf{k}) &= -i\sum_{\mu_m>0}\langle\phi_m(0,\mathbf{k})|\partial_{k_i}|\phi_m(0,\mathbf{k})\rangle.\end{aligned} \tag{3}$$

Due to the $U(1)$ spin rotational symmetry, the Green's function is diagonal with respect to the spin index, thus we can calculate Chern numbers by Eq. (4) for both spin-up and spin-down sectors denoted as $C_\uparrow$ and $C_\downarrow$. Then the spin Chern number C_s is simply defined as $C_s = (C_\uparrow - C_\downarrow)/2$. For 2D time-reversal invariant systems, $C_\uparrow + C_\downarrow = 0$, which results in the relation $C_s = C_\uparrow$, and we only need to calculate Chern number $C_\uparrow$ from the spin-up part of zero-frequency single-particle Green's function $G_\uparrow(0,\mathbf{k})$. This expression of spin Chern number has also been applied in QMC [28] and CDMFT [35] simulations for interacting two-dimensional topological insulators (or the "quantum spin Hall insulators (QSHI)," in the older terminology).

Through a simple derivation from Eqs. (2) and (3), we can arrive at an expression that is numerically more

convenient [6,28]:

$$\mathcal{C} = \frac{1}{2\pi i}\iint_{\mathbf{k}\in BZ} dk_x dk_y \cdot \mathrm{Tr} \times \{P(\mathbf{k})[\partial_{k_x}P(\mathbf{k})\partial_{k_y}P(\mathbf{k}) - \partial_{k_y}P(\mathbf{k})\partial_{k_x}P(\mathbf{k})]\}, \quad (4)$$

where $P(\mathbf{k})$ is a projection operator matrix constructed from eigenvectors $|\phi_m(0,\mathbf{k})\rangle$ of $G_\sigma(0,\mathbf{k})$:

$$P(\mathbf{k}) = \sum_{\mu_m>0} |\phi_m(0,\mathbf{k})\rangle\langle\phi_m(0,\mathbf{k})|. \quad (5)$$

The systems we are dealing with in this paper are all based on honeycomb lattice; the detailed implementation of Eq. (4) on the honeycomb lattice geometry is presented in Appendix A. Turning off interactions, we can observe that Eq. (1) reduces to the Z_2 invariant for free fermion systems defined by Fu and Kane [12], and both Eq. (2) and Eq. (4) reduce to the TKNN invariant (or Chern number) [5,6] for noninteracting systems.

In the next section, we introduce our numerical evaluation scheme of the Z_2 invariant in Eq. (1) and spin Chern number in Eq. (4) in QMC simulations, for model systems of interacting TIs with $U(1)_{\mathrm{spin}} \times U(1)_{\mathrm{charge}} \rtimes Z_2^T$ symmetry and the spatial inversion symmetry. Especially, both Z_2 invariant and spin Chern number for interacting TIs are necessary to be quantized to achieve well-defined topological phases. Thus, both the interpolation technique and implementation of symmetry properties during numerical calculations to reach quantized topological invariants are mainly introduced in the next section.

B. Quantum Monte Carlo method

In this series of work, we apply the projector quantum Monte Carlo (PQMC) simulation [29], which is the zero-temperature version of determinantal QMC algorithm [40]. PQMC method obtains the ground-state observables by carrying out an imaginary time evolution starting from trial wave function that has overlap to the true many-body ground state. The ground-state expectation value of physical observable is calculated as follows,

$$\langle\hat{O}\rangle = \lim_{\Theta\to+\infty} \frac{\langle\psi_T|e^{-\Theta\hat{H}/2}\hat{O}e^{-\Theta\hat{H}/2}|\psi_T\rangle}{\langle\psi_T|e^{-\Theta\hat{H}}|\psi_T\rangle}, \quad (6)$$

where $|\psi_T\rangle$ is the trial wave function and Θ is projection parameter. In all the simulations, to ensure that the algorithm arrives at the truly converged ground state of finite size systems, we choose $\Theta = 40/t$ and $\Delta\tau = 0.05/t$, in which $\Delta\tau$ is the finite imaginary time step applied in the Trotter decomposition of partition function.

We can obtain both the static and dynamic observables. Static ones include the expectation values of energy densities, double occupancy, and spin-spin correlation function. As for the dynamic properties, we can measure the dynamic single-particle Green's function and spin-spin correlation function, from which we can determine both the single-particle gap and spin gap for the many-body systems. Especially, we concentrate on the single-particle Green's function $G_\sigma(\mathbf{k},\tau)$ to calculate the topological invariants. Generally, $G_\sigma(\mathbf{k},\tau)$ (in spin sector σ) is defined as

$$[G_\sigma(\tau,\mathbf{k})]_{pq} = -\frac{1}{N}\sum_{i,j} e^{i\mathbf{k}\cdot(\mathbf{R}_i-\mathbf{R}_j)}\langle T_\tau[c_{ip,\sigma}(\tau)c^\dagger_{jq,\sigma}]\rangle, \quad (7)$$

where $i,j \in [1,N]$ are the unit cell indices and $p,q \in [1,N_o]$ are the orbital indices inside a unit cell. In this manner, for each $\mathbf{k}$ point, $G_\sigma(\tau,\mathbf{k})$ is a $N_o \times N_o$ Hermitian matrix [according to Eq. (12)], and for the $L \times L$ system, there are $N = L^2$ momentum points. From $G_\sigma(\tau,\mathbf{k})$ data, we can directly obtain the single-particle gap. Most importantly, we need to construct the zero-frequency single-particle Green's function $G_\sigma(i\omega = 0,\mathbf{k})$ from $G_\sigma(\tau,\mathbf{k})$ by combining Fourier transformation and symmetry analysis presented in Sec. III, after which the topological invariants can be calculated according to Eqs. (1) and (4).

III. NUMERICAL EVALUATION SCHEME OF TOPOLOGICAL INVARIANTS

This section is divided into four successive parts. First, in Sec. III A, we comment on the condition for zero-frequency single-particle Green's function $G_\sigma(i\omega = 0,\mathbf{k})$ to be well-behaved in both free and interacting fermion systems. Second, in Sec. III B, we explain how to obtain correct $G_\sigma(i\omega = 0,\mathbf{k})$ data from QMC simulation on a finite-size system. Third, Sec. III C clarifies some numerical details in evaluations of Z_2 invariant and spin Chern number. Finally, as the most important part, the interpolation process of $G_\sigma(i\omega = 0,\mathbf{k})$ is introduced in Sec. III D to achieve the ideally quantized topological invariants from QMC simulation in a finite-size system.

A. Condition for well-behaved $G(i\omega = 0,\mathbf{k})$

In this work, we shall be concerned with quantum many-body systems at zero temperature. Suppose that the system under consideration is gapped and has a unique ground state under periodic boundary condition (no intrinsic topological order), thus there is a many-body energy gap Δ between the ground state energy level E_0 and the first excited energy level E_1, namely, $\Delta = E_1 - E_0$. In the Lehmann representation, we can see that the retarded Green's function $G(z,\mathbf{k})$ with complex frequency variable $z = \omega_R + i\omega_I$ is an analytical function in the $\omega_R \in (-\Delta,\Delta)$ region. In fact, the Lehmann representation for $G(z,\mathbf{k})$ at zero temperature reads

$$G_{\alpha\beta}(z,\mathbf{k}) = \sum_{m\neq 0}\left[\frac{\langle 0|c_{\mathbf{k}\alpha}|m\rangle\langle m|c^\dagger_{\mathbf{k}\beta}|0\rangle}{z-(E_m-E_0)} + \frac{\langle m|c_{\mathbf{k}\alpha}|0\rangle\langle 0|c^\dagger_{\mathbf{k}\beta}|m\rangle}{z+(E_m-E_0)}\right]. \quad (8)$$

Since the condition $E_m - E_0 \geqslant \Delta$ is satisfied, $G(z,\mathbf{k})$ has no poles in the $\omega_R \in (-\Delta,\Delta)$ region on the real axis. We can further observe that $G(z,\mathbf{k})$ is actually an analytical function with $\omega_R \in (-\Delta,\Delta)$ and arbitrary ω_I. Topological invariants are defined in terms of zero-frequency Green's function, namely, the Green's function at $z = 0$. More precisely, since the chemical potential has been absorbed into the definition of E_m (namely, E_m is the eigenvalue of $\hat{H} - \mu\hat{N}$, where $\hat{N}$ is the particle number operator and μ is the chemical potential), the zero frequency refers to the energy exactly at the chemical potential [21]. Tuning the chemical potential within the energy

gap is harmless in an insulator. Thus, the zero-frequency single-particle Green's function is well defined for TIs with the above mentioned properties at zero temperature, and one can construct topological invariants from it.

From both Eq. (1) and Eq. (4), we can determine that there are two scenarios of the jumping of topological invariants determined in terms of Green's function. The first scenario is the pole of Green's function, which is the conventional case, and the topological transitions in noninteracting fermion systems belong to this class. The second scenario is the zero of Green's function (namely, an eigenvalue of the Green's function matrix becomes zero). From the Lehmann representation, we can see that the first scenario must describe a phase transition, since $E_m - E_0 = 0$ implies gap closing. On the other hand, the second scenario can be a topological phase transition [17,23], but it is not necessarily so.

B. Calculations of $G(i\omega = 0,\mathbf{k})$

In QMC, we measure the imaginary-time displaced Green's function $G(\tau,\mathbf{k})$ and obtain $G(i\omega_n,\mathbf{k})$ by Fourier transformation as follows

$$G(i\omega_n,\mathbf{k}) = \int_0^\beta d\tau e^{i\omega_n\tau} G(\tau,\mathbf{k}). \tag{9}$$

Note that Eq. (9) has already incorporated the antiperiodic condition for $G(\tau,\mathbf{k})$ as $G(\tau+\beta,\mathbf{k}) = -G(\tau,\mathbf{k})$. However, Eq. (9) is only valid for finite temperature. At zero temperature, $i\omega_n$ becomes continuous on the imaginary frequency axis and the antiperiodic condition for $G(\tau,\mathbf{k})$ is not quite meaningful. In such a case, one needs to apply the following Fourier transformation

$$G(i\omega,\mathbf{k}) = \int_{-\infty}^{+\infty} d\tau e^{i\omega\tau} G(\tau,\mathbf{k}). \tag{10}$$

The validity of using Eq. (10) at zero temperature is presented in Appendix B. From Eq. (10), we can directly obtain the zero-frequency single-particle Green's function $G(i\omega,\mathbf{k})$ by substituting $i\omega = 0$ as,

$$G(i\omega = 0,\mathbf{k}) = \int_{-\infty}^{+\infty} d\tau G(\tau,\mathbf{k}). \tag{11}$$

One can furthermore make use of the symmetry properties of $G(\tau,\mathbf{k})$ to simplify the calculation. For a general multiband system with N_O orbitals (in each spin sector within a unit cell), one can prove

$$[G_\sigma(\tau,\mathbf{k})]_{pq} = [G_\sigma(\tau,\mathbf{k})]^\star_{qp} \tag{12}$$

with $p,q \in [1,N_O]$. Equation (12) explicitly shows that $G_\sigma(\tau,\mathbf{k})$ is a $N_O \times N_O$ Hermitian matrix. If the system preserves spatial inversion symmetry and the corresponding spatial inversion operation transforms p sublattice to p' sublattice, then we can prove

$$[G_\sigma(\tau,\mathbf{k})]_{pq} = [G_\sigma(\tau,-\mathbf{k})]_{p'q'}. \tag{13}$$

Equation (13) explicitly connects the $G_\sigma(\tau,\mathbf{k})$ data with opposite wave-vector points. If the system preserves particle-hole symmetry, we can prove

$$[G_\sigma(\tau,\mathbf{k})]_{pq} = -\xi_p\xi_q[G_\sigma(-\tau,-\mathbf{k})]_{qp}, \tag{14}$$

where ξ_p and ξ_q are the sign change during on-site particle-hole transformation as $c_p \to \xi_p c_p^\dagger$ and $c_q \to \xi_q c_q^\dagger$. Equation (14) shows the connections of $G_\sigma(\tau,\mathbf{k})$ data with positive and negative τ. The detailed proof for Eqs. (12), (13), and (14) is demonstrated in Appendix C. Combining these three symmetry properties of the $G_\sigma(\tau,\mathbf{k})$ matrix, we can determine that the number of nonzero and independent matrix elements in $G_\sigma(\tau,\mathbf{k})$ is much smaller than N_O^2.

C. Numerical details in evaluating topological invariants

Besides the discussions in Secs. III A and III B, there are still some important details in numerical application of Eq. (4) for calculating the topological invariants. Firstly, the infinite integral over imaginary time τ in Eq. (11) can be approximated by a cutoff θ as

$$G(i\omega = 0,\mathbf{k}) \approx \int_{-\theta}^{+\theta} d\tau G(\tau,\mathbf{k}). \tag{15}$$

For TIs, the systems have $G_\sigma(\tau,\mathbf{k}) \propto e^{-\Delta_{sp}(\mathbf{k})\tau}$ at large τ with $\Delta_{sp}(\mathbf{k})$ as the single-particle gap at $\mathbf{k}$ point. If the gap $\Delta_{sp}(\mathbf{k})$ is large, the exponential decay of $G_\sigma(\tau,\mathbf{k})$ in imaginary time will be very fast, and a finite θ is sufficient for the system to evolve below the energy scale of Δ_{sp}. However, this approximation can induce considerable error around the topological phase transition with single-particle gap closing, since the decaying of $G_\sigma(\tau,\mathbf{k})$ is very slow around the transition point. Later on, one will observe the nonmonotonic behavior in results of Chern number $C_\uparrow$ close to the topological phase transition points in Sec. IV, which is originating from the above τ cutoff. We then calculate the integral in Eq. (15) numerically by a simple trapezoidal method, and the step size for this simple method is actually the $\Delta\tau$ used in QMC simulations.

Secondly, the first-order derivatives over k_x,k_y in Eq. (4) are replaced by first-order finite difference [28]. Since the interval between two adjacent $\mathbf{k}$ points is proportional to $1/L$ for a $L \times L$ system, replacing the derivatives by finite-difference will bring in error proportional to $1/L$, which is the key origin for finite-size effect in Chern number calculated by Eq. (4). Also, the integral over $\mathbf{k}$ in the BZ region in Eq. (4) can only be performed by summations over L^2 discrete $\mathbf{k}$ points for a $L \times L$ system. We can imagine this can also contribute to finite-size effect in Chern number calculation by Eq. (4). Overall, due to the finite-size effect in QMC simulations, the spin Chern number result can be very far from the expected integer [28].

D. Interpolation of $G(i\omega = 0,\mathbf{k})$

As discussed above, the spin Chern number calculated from QMC simulations in finite-size systems suffer severe finite-size effect, and the obtained results are usually far away from the expected integer values. To remove the finite-size effect, we propose an interpolation process for $G(i\omega = 0,\mathbf{k})$ to obtain integer-quantized spin Chern number.

We emphasize that the calculation of Chern number by Eq. (A7) in Appendix A from QMC data of $G(i\omega = 0,\mathbf{k})$ for $L \times L$ systems actually adopts the linear interpolation of $G(i\omega = 0,\mathbf{k})$ in the whole BZ region, since there are actually only L^2 accessible $\mathbf{k}$ points during simulations with

periodic boundary conditions (PBC). That linear interpolation introduces systematic error proportional to $1/L$, which is the origin of finite-size effect for spin Chern number. Then we can imagine that via obtaining numerical data of $G(i\omega = 0,\mathbf{k})$ at more $\mathbf{k}$ points can surely suppress the finite-size effect. The method for that is naturally to apply twisted boundary conditions (TBC) with phases (θ_1,θ_2) in $(\mathbf{a}_1,\mathbf{a}_2)$ directions during the QMC simulations for a fixed $L \times L$ system. Implementing twisted boundary conditions during QMC simulations actually corresponds to shifting the accessible $\mathbf{k}$ points in BZ region, which allows one to obtain data of $G(i\omega = 0,\mathbf{k})$ at other $\mathbf{k}$ points beside the L^2 $\mathbf{k}$ points under PBC. However, practical QMC simulations with TBC can cause much heavier computational effort, since different twisted boundary phases shall be used. Instead, we put forward an interpolation process for $G(i\omega = 0,\mathbf{k})$ based on its data at L^2 accessible $\mathbf{k}$ points under PBC.

The procedures of the interpolation process and corresponding calculations of spin Chern number are as following. First, we carry out the QMC simulations under PBC for a $L \times L$ system with N_O orbitals inside a unit cell (for one spin sector). Second, we obtain the data of $G(i\omega = 0,\mathbf{k})$ at L^2 $\mathbf{k}$ points by Eq. (15). After that we carry out the Fourier transformation for $G(i\omega = 0,\mathbf{k})$ to get the real space $[G_{\sigma,ij}(i\omega = 0)]_{pq}$ data. Then, we obtain $G_\sigma(i\omega = 0,\mathbf{k})$ data at arbitrary $\mathbf{k}$ point in BZ by

$$[G_\sigma(0,\mathbf{k})]_{pq} = \frac{1}{L^2}\sum_{i,j=1}^{L^2}[G_{\sigma,ij}(i\omega = 0)]_{pq}e^{i\mathbf{k}\cdot(\mathbf{R}_i-\mathbf{R}_j)}, \qquad (16)$$

where i,j stands for unit cells and $p,q \in [1,N_O]$ are the indexes for orbital or band. Eq. (16) is applied here according to the periodization process in CDMFT, which is presented in detail in Appendix D. Mathematically, the above process by Eq. (16) for $G_\sigma(i\omega = 0,\mathbf{k})$ is actually the trigonometric function interpolation, which is very appropriate for periodic function like $G_\sigma(i\omega = 0,\mathbf{k})$ (see more details in Appendix D). Here, we need to admit that other interpolation methods instead of above procedure can also be applied to obtain $G_\sigma(i\omega = 0,\mathbf{k})$ data at more $\mathbf{k}$ points. However, the above interpolation process we have adopted is extremely simple to be implemented numerically. Comparing to other interpolation methods, which are actually simple fittings of $G_\sigma(i\omega = 0,\mathbf{k})$ curve over $\mathbf{k}$ points in BZ region, interpolation of $G_\sigma(i\omega = 0,\mathbf{k})$ by above process is physically more reasonable. Beside the fact that the above interpolation process only deals with simple discrete Fourier transformations already used in CDMFT, it also makes $G_\sigma(i\omega = 0,\mathbf{k})$ differential to any order at arbitrary $\mathbf{k}$ point. The validity of the interpolation process is based on the observation that the topology of the system will not change during a continuous deformation if there is no gap closing, which makes the interpolation process natural and appropriate. This means that if the continuous deformation do not generate any singularity of the single-particle Green's function, the interpolation process will not alter the topological property of the system, but only improve the quality of the calculated topological invariants and allow us to achieve quantized spin Chern number. Conclusively, the above interpolation process for $G(i\omega = 0,\mathbf{k})$ can be approximately taken as carrying out QMC simulations with TBC to obtain $G(i\omega = 0,\mathbf{k})$ data at different $\mathbf{k}$ points in BZ region physically, while it's interpolation mathematically.

During practical QMC simulations, the lattice size for interpolation process will be large but still finite, and then we choose the interpolation lattice size $IL \times IL$ and construct the $G_\sigma(i\omega = 0,\mathbf{k})$ data at $IL \times IL$ wavevector points in BZ by Eq. (16). IL can be much bigger than original lattice size L in QMC simulation. Then we evaluate the spin Chern number for the $IL \times IL$ system by Eq. (A7) in Appendix A. In next section, one can clearly observe the converging of spin Chern number to the ideal quantized value with increasing IL.

IV. APPLICATIONS IN QMC

In this section, we apply the above mentioned numerical scheme to two independent 2D interacting TIs. The topological phase transitions in these systems are driven by single-particle parameters. Results of topological invariants across topological phase transitions in generalized Kane-Mele-Hubbard model (GKMH) are shown in Sec. IV A, while Sec. IV B concentrates on topological phase transitions in the cluster Kane-Mele-Hubbard model (CKMH).

We set the following parameters in the QMC simulations, $\Theta = 40/t, \Delta\tau = 0.05/t$. For the imaginary time integration in Eq. (15), a cutoff $\theta = 20/t$ is applied.

A. Generalized Kane-Mele-Hubbard model

Generalized Kane-Mele-Hubbard (GKMH) model [26,28,29] is given by

$$\begin{aligned}\hat{H} = &-t\sum_{\langle i,j\rangle\sigma} t_{ij}(c^\dagger_{i\sigma}c_{j\sigma} + h.c) - t_3\sum_{\langle\langle\langle i,j\rangle\rangle\rangle\sigma}(c^\dagger_{i\sigma}c_{j\sigma} + \text{H.c.})\\ &+ i\lambda\sum_{\langle\langle i,j\rangle\rangle\alpha\beta}\nu_{ij}\left(c^\dagger_{i\alpha}\sigma^z_{\alpha\beta}c_{j\beta} - c^\dagger_{j\beta}\sigma^z_{\beta\alpha}c_{i\alpha}\right)\\ &+ \frac{U}{2}\sum_i(n_{i\uparrow} + n_{i\downarrow} - 1)^2. \qquad (17)\end{aligned}$$

For nearest-neighbor (NN) hopping, we have $t_{ij} = t_d$ for NN bonds inside unit cells and $t_{ij} = t$ for the others, as demonstrated in Fig. 1(a). The t_3 term is the third-nearest-neighbor hopping. The fourth term represents spin-orbit coupling (λ) connecting next-nearest-neighbor sites with a complex (time-reversal symmetric) hopping. The factor $\nu_{ij} = -\nu_{ji} = \pm 1$ depends on the orientation of the two nearest-neighbor bonds that the electron moves in going from site i to j. The last term describes the on-site Coulomb repulsion. For the GKMH model, we set t as energy unit.

Due to the $U(1)_{\text{spin}} \times U(1)_{\text{charge}} \rtimes Z_2^T$ symmetry of the system, the GKMH model acquires a $\mathbb{Z}$ classification. Without interaction ($U = 0$), the $(t_d/t) - (t_3/t)$ phase diagram for $\lambda/t > 0$, determined from both Z_2 invariant $(-1)^\nu$ and Chern number C_s, is shown in Fig. 2(a). There are four phases and their phase boundaries in Fig. 2(a) are independent of the size of λ/t, as long as $\lambda/t > 0$. In Fig. 2(b), we show the spin Chern number $C_\uparrow$ for fixed $t_d/t = 0.5$ and increasing t_3/t, calculated from Eq. (4). Since the system is noninteracting, we have $G_\sigma(i\omega = 0,\mathbf{k}) = -[\mathcal{H}_\sigma(\mathbf{k})]^{-1}$ with $\mathcal{H}_\sigma(\mathbf{k})$ the 2×2 noninteracting Hamiltonian matrix for the GKMH model. In Fig. 2(b), one can clearly observe that the Chern number C_s

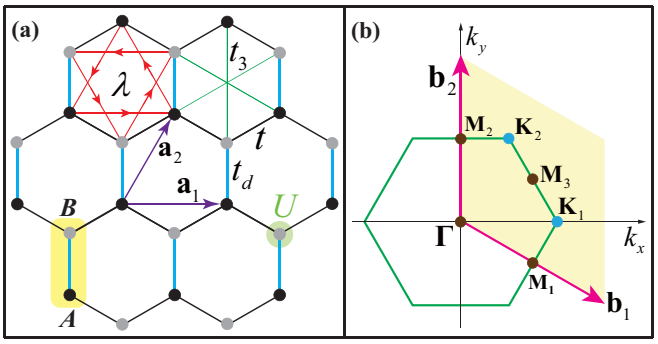

FIG. 1. (a) Illustration of the GKMH model as in Eq. (17). The unit cell is presented as the yellow shaded rectangle, consisting of A and B sublattices denoted by black and gray dots. The lattice is spanned by primitive vectors $\mathbf{a}_1 = (\sqrt{3},0)a, \mathbf{a}_2 = (1/2,\sqrt{3}/2)a$ with a the lattice constant. The black and blue lines denote nearest-neighbor hopping t and t_d, while the λ term and third-nearest-neighbor hopping t_3 are represented by red and green lines. The arrows in red lines shows $\nu_{ij} = +1$ for spin-up part. (b) BZ of GKMH model. $\mathbf{K}_1, \mathbf{K}_2$ are Dirac points, while $\boldsymbol{\kappa} = \Gamma, \mathbf{M}_1, \mathbf{M}_2, \mathbf{M}_3$ are the four TRIM points.

converges to its expected quantized value, with increasing lattice size.

With finite interaction strength U, we need to measure the single-particle Green's function $G_\sigma(\tau,\mathbf{k})$ in QMC simulation and then construct the topological invariants from it. For the GKMH model, $G_\sigma(\tau,\mathbf{k})$ is a 2×2 Hermitian matrix, according to Eq. (12). Due to the presence of spatial inversion symmetry and Eq. (13), we can obtain $[G_\sigma(\tau,\mathbf{k})]_{11} = [G_\sigma(\tau,-\mathbf{k})]_{22}$ and $[G_\sigma(\tau,\mathbf{k})]_{12} = [G_\sigma(\tau,-\mathbf{k})]_{21}$. Then at TRIM points $\boldsymbol{\kappa}$, we have $[G_\sigma(\tau,\boldsymbol{\kappa})]_{11} = [G_\sigma(\tau,\boldsymbol{\kappa})]_{22}$ and $[G_\sigma(\tau,\boldsymbol{\kappa})]_{12} = [G_\sigma(\tau,\boldsymbol{\kappa})]_{21}$. From Eq. (14), we can get $[G_\sigma(\tau,\mathbf{k})]_{pp} = -[G_\sigma(-\tau,-\mathbf{k})]_{pp}, p = 1,2$ and $[G_\sigma(\tau,\mathbf{k})]_{12} = [G_\sigma(-\tau,-\mathbf{k})]_{21}$. Combining these relations, we obtain the equations applied in numerical calculations as $[G_\sigma(-\tau,\mathbf{k})]_{11} = -[G_\sigma(\tau,\mathbf{k})]_{22}, [G_\sigma(-\tau,\mathbf{k})]_{12} = [G_\sigma(\tau,\mathbf{k})]_{12}$. At TRIM points, $G_\sigma(\tau,\boldsymbol{\kappa})$ is a real symmetric matrix with equal diagonal elements. Based on these considerations, we deduce that there are only two independent matrix elements in $G_\sigma(\tau,\mathbf{k})$ as

$$[G_\sigma(i\omega=0,\mathbf{k})]_{11} = -[G_\sigma(i\omega=0,\mathbf{k})]_{22} \approx \int_0^{+\theta} \{[G_\sigma(\tau,\mathbf{k})]_{11} - [G_\sigma(\tau,\mathbf{k})]_{22}\} d\tau, \quad (18)$$

and

$$[G_\sigma(i\omega=0,\mathbf{k})]_{12} = [G_\sigma(i\omega=0,\mathbf{k})]^\star_{21} \approx 2\int_0^{+\theta} [G_\sigma(\tau,\mathbf{k})]_{12} d\tau. \quad (19)$$

As mentioned above, θ is the cutoff for τ in the integral of Eq. (13). Equations (18) and (19) explicitly show that we only need to measure two elements of $G_\sigma(\tau,\mathbf{k})$ matrix with $\tau > 0$ at all discrete $\mathbf{k}$ points. At TRIM points, we can obtain the simplified relations as $[G_\sigma(i\omega=0,\boldsymbol{\kappa})]_{11} = [G_\sigma(i\omega=0,\boldsymbol{\kappa})]_{22} = 0$ and $[G_\sigma(i\omega=0,\boldsymbol{\kappa})]_{12} = [G_\sigma(i\omega=0,\boldsymbol{\kappa})]_{21}$. Namely, at TRIM points we have $G_\sigma(i\omega=0,\boldsymbol{\kappa}) = Z_{\boldsymbol{\kappa}}\sigma_x$ while σ_x is the Pauli matrix and $Z_{\boldsymbol{\kappa}}$ is some $\boldsymbol{\kappa}$-dependent coefficient [26–29].

For Z_2 invariant, we only deal with $G_\sigma(i\omega=0,\boldsymbol{\kappa})$. The matrix representation of inversion symmetry operator $\hat{P}$ for the GKMH model is $P = \sigma_x$ for each spin sector. The parity of all unoccupied eigenstates at some TRIM point $\boldsymbol{\kappa}$ is simply $\eta(\boldsymbol{\kappa}) = \mathrm{sgn}\{[G_\sigma(0,\boldsymbol{\kappa})]_{12}\}$. Then we can get the Z_2 invariant simply as $(-1)^\nu = \eta(\boldsymbol{\Gamma})\eta(\mathbf{M}_1)\eta(\mathbf{M}_2)\eta(\mathbf{M}_3)$. As a result, we observe that the Z_2 invariant for the GKMH model is integer-quantized, free from finite-size effect. On the other hand, to calculate spin Chern number C_s, we only need to obtain $[G_\sigma(\tau,\mathbf{k})]_{11}$ and $[G_\sigma(\tau,\mathbf{k})]_{12}$ in $G_\sigma(\tau,\mathbf{k})$ matrix due to its Hermiticity. After that, spin Chern number can be numerically evaluated through Eq. (4).

To apply our numerical calculation scheme for topological invariants, we choose two paths in the phase diagram of Fig. 2(a). First, starting from $t_d/t = 1.0, \lambda/t = 0.2$ and $U/t = 2.0$, we calculate the topological invariants to monitor the t_3-driven topological phase transition. Second, we choose $t_3/t = 0, \lambda/t = 0.2, U/t = 2.0$ and calculate the topological invariants to monitor the t_d-driven topological phase transition. The interaction is chosen to be at a small value $U/t = 2.0$ to avoid the appearance of antiferromagnetic state [29,41]. Thus, there is no spontaneous symmetry breaking across these two topological phase transitions driven by hopping parameters in the interacting GKMH model.

For the t_3-driven topological phase transition, the results of both Z_2 invariant and Chern number $C_\uparrow$ (equal to spin Chern number C_s) from QMC simulations with finite size

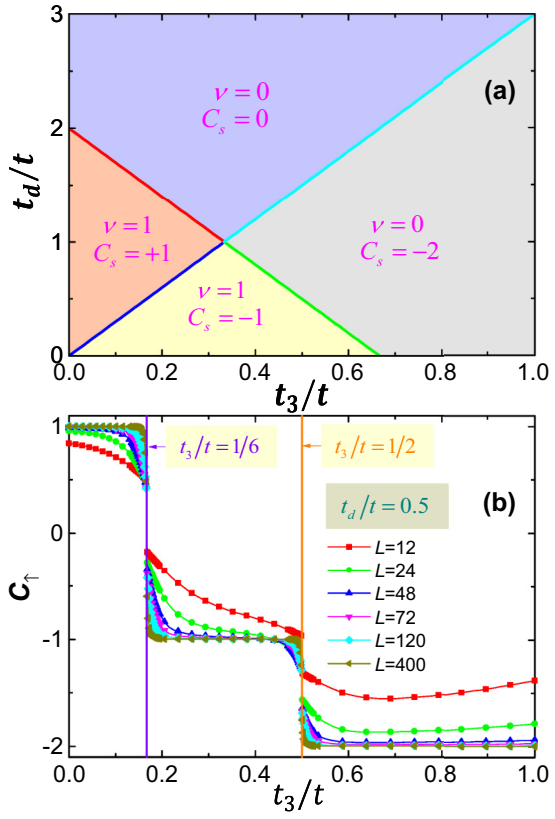

FIG. 2. (a) $(t_d/t) - (t_3/t)$ Phase diagram for GKMH model at $U = 0$ and arbitrary $\lambda/t > 0$. (b) Calculation results of Chern number $C_\uparrow$ with $t_d/t = 0.5$ and varying t_3/t, the linear system sizes are $L = 12,24,48,72,120,400$.

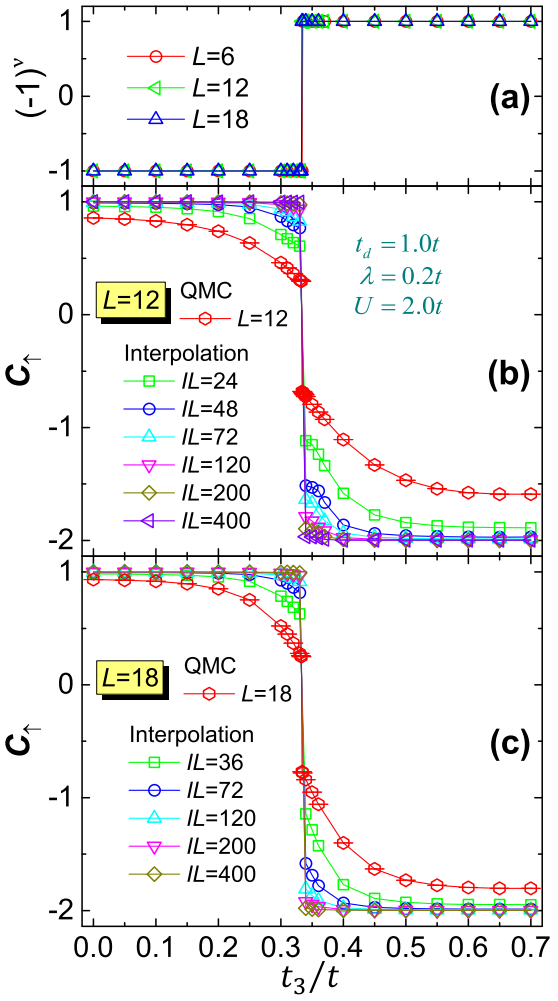

FIG. 3. (a) Z_2 invariant $(-1)^{\nu}$ and (b), (c) Chern number $C_{\uparrow}$ for the t_3-driven topological phase transition in the GKMH model with $t_d/t = 1.0, \lambda/t = 0.2$ and $U/t = 2.0$ from finite-size QMC simulation and the interpolation process. (a) Z_2 invariant $(-1)^{\nu}$ is quantized as mentioned in the main text. (b) and (c), the Chern number $C_{\uparrow}$ from finite-size QMC calculation indicated by the red open hexagon with error bar acquires a drop with finite value at the transition point, which can be taken as signature of topological phase transition, but the $C_{\uparrow}$ itself is not quantized before or after the phase transition, due to the finite-size effect. After the interpolation with the QMC data in $L = 12$ (b) and $L = 18$ (c) systems, the $C_{\uparrow}$ converge to the ideal quantized integers, where lL stands for interpolation lattice size used in the interpolation process.

$L = 6, 12, 18$ are shown in Figs. 3(a), 3(b), and 3(c), at $t_d/t = 1.0, \lambda/t = 0.2$ and $U/t = 2.0$. At $U = 0$, the GKMH model experiences a topological phase transition at $t_3/t = 1/3$ from $C_s = +1$ to $C_s = -2$ as indicated in Fig. 2(a). At $U/t = 2.0$, the quantized Z_2 invariant in Fig. 3(a) demonstrates that the topological phase transition point changes little. Detailed calculations of parities at all TRIM points show that the parities at $\mathbf{M}_1, \mathbf{M}_2, \mathbf{M}_3$ change across the phase transition, which is related to the fact that the single-particle gap closes at $\mathbf{M}_1, \mathbf{M}_2, \mathbf{M}_3$ points [29]. As for the Chern number from finite-size QMC calculation denoted by the red open hexagon symbols with error bar in Figs. 3(b) and 3(c), we can observe drop with finite values across the phase transition, the position coincide with that in Z_2 invariant. Combining these results, the phase transition point is $t_3/t \approx 0.334 \sim 0.335$ for the $L = 6$ system and $t_3/t \approx 0.333 \sim 0.334$ for the $L = 12, 18$ system.

The problem about the results of Chern number in Figs. 3(b) and 3(c) is that they are not integer quantized, though the convergence with increasing L can be observed. To solve this problem, the interpolation process described in Sec. III D is applied based on the results of Chern number from QMC simulations of $L = 12, 18$. As shown in Figs. 3(b) and 3(c), one indeed observes the gradual convergence of Chern number $C_{\uparrow}$ when the interpolation lattice size lL increases. In fact, for $lL = 120$, the Chern number $C_{\uparrow}$ is almost ideally quantized, which demonstrates that the interpolation method works very well. Numerical results for the t_d-driven topological phase transition, which are presented in Appendix F, show similar effectiveness of our numerical evaluation scheme of the topological invariants.

B. Cluster Kane-Mele-Hubbard model

The cluster Kane-Mele-Hubbard model [30,42] (CKMH) has six honeycomb lattice sites as one unit cell; the Hamiltonian is given as follows

$$\begin{aligned}\hat{H} = &-\sum_{\langle ij\rangle\sigma} t_{ij}(c^{\dagger}_{i\sigma}c_{j\sigma} + c^{\dagger}_{j\sigma}c_{i\sigma}) \\ &+ i\lambda_I \sum_{\langle\langle ij\rangle\rangle\alpha\beta} \nu_{ij}\left(c^{\dagger}_{i\alpha}\sigma^{z}_{\alpha\beta}c_{j\beta} - c^{\dagger}_{j\beta}\sigma^{z}_{\beta\alpha}c_{i\alpha}\right) \\ &+ i\lambda_O \sum_{\langle\langle ij\rangle\rangle\alpha\beta} \nu_{ij}\left(c^{\dagger}_{i\alpha}\sigma^{z}_{\alpha\beta}c_{j\beta} - c^{\dagger}_{j\beta}\sigma^{z}_{\beta\alpha}c_{i\alpha}\right) \\ &+ \frac{U}{2}\sum_{i}(n_{i\uparrow} + n_{i\downarrow} - 1)^2 \,. \end{aligned} \tag{20}$$

For nearest-neighbor (NN) hopping, we have $t_{ij} = t$ for NN bonds inside unit cells and $t_{ij} = t_d$ for those connecting the six-site unit cells, as demonstrated in Fig. 4(a). The amplitudes for SOC term inside a unit cell and between different unit cells are λ_I and λ_O, respectively. U is the on-site Coulomb repulsion. Similar to the GKMH model, the $U(1)_{\text{spin}} \times U(1)_{\text{charge}} \rtimes Z_2^T$ symmetry is also preserved in the CKMH model, which results in $\mathbb{Z}$ classification. Besides, both spatial inversion symmetry and particle-hole symmetry are also present in the CKMH model. Notice that the CKMH model has a six-site unit cell, in this section, the linear system size L in finite size QMC simulation actually corresponds to that of the six-site unit cell, i.e., the total lattice sites are $6 \times L \times L$. The physical origin of the CKMH model is actually the Kekulé distortion, which explicitly breaks the transitional symmetry of honeycomb lattice and trigger cluster anisotropy in hopping strengths. Such a large unit cell greatly increases the QMC simulation efforts of the CKMH model comparing to that of the GKMH model in the previous session, where the total lattice site is only $2 \times L \times L$ (the computation efforts of QMC scale to the third power of the total lattice sites).

Since there are three independent parameters $t_d, \lambda_I, \lambda_O$, even the phase diagram for the noninteracting CKMH model is already interesting. To simplify the presentation, we only demonstrate results on two special cases. First, we set $\lambda_O = 0$,

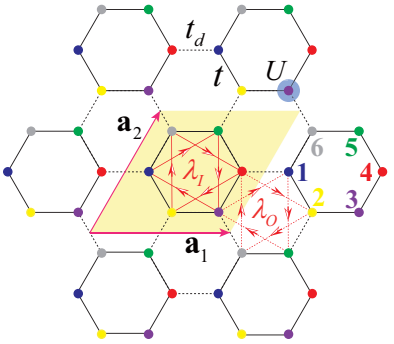

FIG. 4. Illustration of the CKMH model in Eq. (20). The yellow shaded region shows the six-site unit cell with primitive lattice vectors $\mathbf{a}_1 = (\sqrt{3},0)a, \mathbf{a}_2 = (1/2,\sqrt{3}/2)a$ with the nearest-neighbor bond length $a/\sqrt{3}$. The six sublattices 1,2,3,4,5,6 are shown in different colors. The black solid and black dotted lines indicate the nearest-neighbor hopping term inside (t) and between (t_d) unit cells. The red solid and red dotted lines represent SOC terms inside (λ_I) and between (λ_O) unit cells. The sign choice for SOC hopping is the same as that in Fig. 1(a). The on-site Coulomb repulsion U is shown by the blue shaded circle.

the $(t_d/t) - (\lambda_I/t)$ phase diagram of this case is shown in Fig. 5(a). We can observe that the QSHI phases exist in the middle region of the $(t_d/t) - (\lambda_I/t)$ phase diagram, with different spin Chern numbers $C_s = +1$ and $C_s = -2$, as a function of λ_I/t. The presence of the $C_s = -2$ phase is unexpected and very interesting, since the Chern number is

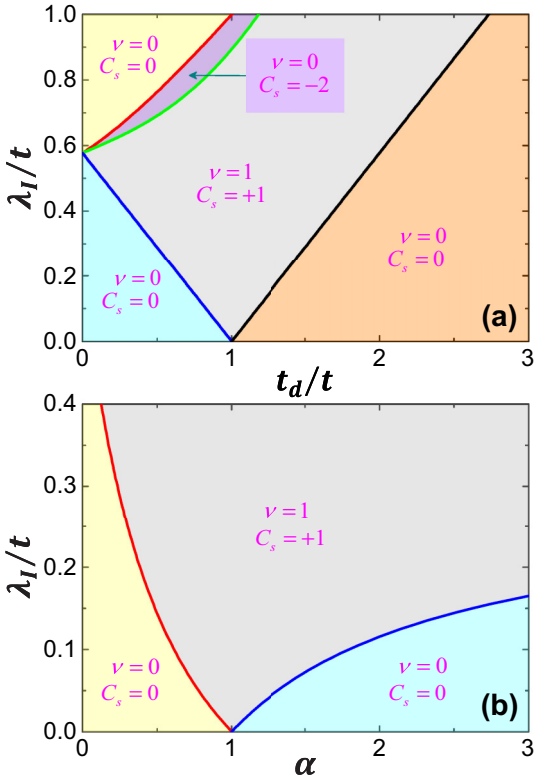

FIG. 5. Phase diagrams for the noninteracting CKMH model under two different parameter sets. (a) $(t_d/t) - (\lambda_I/t)$ phase diagram with $\lambda_O = 0$; (b) $\alpha - (\lambda_I/t)$ phase diagram with $\alpha = t_d/t = \lambda_O/\lambda_I$.

changed by 3 when going from $C_s = 1$ to $C_s = -2$, further increase λ_I/t, QSHI phase is destroyed. Second, we keep all three t_d,λ_I,λ_O parameters finite and introduce a ratio of hopping $\alpha = t_d/t = \lambda_O/\lambda_I$. The $\alpha - (\lambda_I/t)$ phase diagram at $U = 0$ is presented in Fig. 5(b). In the plotted region of α and t_d/t, three phases with one nontrivial in C_s are found.

With interaction, we apply the interpolation process in Sec. III D to calculate the topological invariants. Before presenting the data, let's discuss the structure of $G_\sigma(\tau,\mathbf{k})$ and $G_\sigma(i\omega = 0,\mathbf{k})$ for the CKMH model as it is quite complicated. First, both $G_\sigma(\tau,\mathbf{k})$ and $G_\sigma(i\omega = 0,\mathbf{k})$ are 6×6 Hermitian matrices for the CKMH model. Second, using spatial inversion and particle-hole symmetries, we can obtain useful relations among the matrix elements of $G_\sigma(\tau,\mathbf{k})$. Combining these two symmetry properties, $G_\sigma(\tau,\mathbf{k})$ and $G_\sigma(-\tau,\mathbf{k})$ are explicitly related and we only need to calculate the $G_\sigma(\tau,\mathbf{k})$ data with $\tau > 0$. The detailed analysis is presented in Appendix E. The $G_\sigma(i\omega = 0,\mathbf{k})$ matrix for the CKMH model only has 12 independent matrix elements and can be expressed as

$$G_\sigma(0,\mathbf{k}) = \begin{pmatrix} A_1 & A_4 & A_5 & A_6 & A_7 & A_8 \\ A_4^\star & A_2 & A_9 & -A_7 & A_{10} & A_{11} \\ A_5^\star & A_9^\star & A_3 & A_8 & -A_{11} & A_{12} \\ A_6^\star & -A_7^\star & A_8^\star & -A_1 & A_4^\star & -A_5^\star \\ A_7^\star & A_{10}^\star & -A_{11}^\star & A_4 & -A_2 & A_9^\star \\ A_8^\star & A_{11}^\star & A_{12}^\star & -A_5 & A_9 & -A_3 \end{pmatrix}, \tag{21}$$

where A_1,A_2,A_3 are real numbers and $A_i, i = 4,\ldots,12$ are complex numbers. At TRIM points, Eq. (21) can be further simplified to only 9 independent matrix elements and $G_\sigma(i\omega = 0,\boldsymbol{\kappa})$ matrix obtains the following matrix structure as

$$G_\sigma(0,\boldsymbol{\kappa}) = \begin{pmatrix} 0 & B_4 & iB_5 & B_6 & iB_7 & B_8 \\ B_4 & 0 & B_9 & -iB_7 & B_{10} & iB_{11} \\ -iB_5 & B_9 & 0 & B_8 & -iB_{11} & B_{12} \\ B_6 & iB_7 & B_8 & 0 & B_4 & iB_5 \\ -iB_7 & B_{10} & iB_{11} & B_4 & 0 & B_9 \\ B_8 & -iB_{11} & B_{12} & -iB_5 & B_9 & 0 \end{pmatrix}. \tag{22}$$

In Eq. (22), $B_i, i = 4,\ldots,12$ are real numbers. The explicit expressions for both A_i and B_i are given in Appendix E.

For numerical evaluation of Z_2 invariant in CKMH model, we adopt the $G_\sigma(i\omega = 0,\boldsymbol{\kappa})$ matrix in Eq. (22) for TRIM points. The matrix representation of spatial inversion symmetry operator for each spin sector is

$$P = \begin{pmatrix} 0 & 0 & 0 & 1 & 0 & 0 \\ 0 & 0 & 0 & 0 & 1 & 0 \\ 0 & 0 & 0 & 0 & 0 & 1 \\ 1 & 0 & 0 & 0 & 0 & 0 \\ 0 & 1 & 0 & 0 & 0 & 0 \\ 0 & 0 & 1 & 0 & 0 & 0 \end{pmatrix}. \tag{23}$$

To calculate the Z_2 invariant, we only need to diagonalize the $G_\sigma(i\omega = 0,\boldsymbol{\kappa})$ matrix with $\boldsymbol{\kappa} = \boldsymbol{\Gamma},\mathbf{M}_1,\mathbf{M}_2,\mathbf{M}_3$, and then calculate the parities at these TRIM points by Eq. (1). To calculate spin Chern number, we only need to adopt the matrix structure of $G_\sigma(i\omega = 0,\mathbf{k})$ in Eq. (21) and apply Eq. (4), first

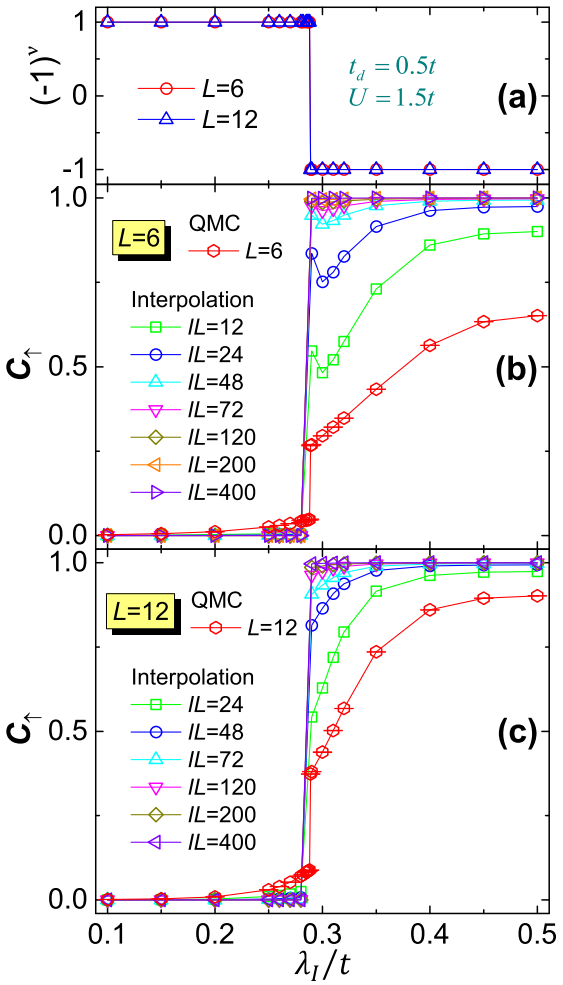

FIG. 6. (a) Z_2 invariant $(-1)^\nu$ and (b), (c) Chern number $C_\uparrow$ for the λ_I-driven topological phase transition with $\lambda_O = 0, t_d/t = 0.5$ and $U/t = 1.5$ from finite-size calculations by QMC simulation (denoted by red open hexagon with error bar) and interpolation process. The drop of integer-valued Z_2 invariant and the jump of Chern number $C_\uparrow$ can be taken as signature of topological phase transition. In (b) and (c), with large interpolation lattice size IL from finite QMC data with $L = 6$ and 12, the Chern number $C_\uparrow$ reaches its quantized value.

with the finite-size QMC data and then with interpolation process.

We concentrate on two independent paths in the parameter space of the CKMH model. First, we choose $\lambda_O = 0, t_d/t = 0.5$ and $U/t = 1.5$ and study the λ_I-driven topological phase transition in the interacting CKMH model. For $U = 0$, the transition point for this λ_I-driven topological phase transition from $C_s = 0$ to $C_s = +1$ is at $\lambda_I/t \approx 0.289$. Second, we set $\alpha = 1.8, U/t = 2.0$ in the CKMH model and study the λ_I-driven topological phase transition, similarly, there is also a λ_I-driven topological phase transition from $C_s = 0$ to $C_s = +1$ at $\lambda_I/t \approx 0.1$ for $U = 0$. In the following, we calculate Z_2 invariant $(-1)^\nu$ and spin Chern number C_s for λ_I/t parameter across these two phase transitions, to demonstrate that our interpolation process works for the CKMH model as well.

Figure 6 shows the Z_2 invariant $(-1)^\nu$ and Chern number $C_\uparrow$ (equal to spin Chern number C_s), calculated from finite-size QMC simulations of $L = 6, 12$ systems (both denoted by red open hexagon with error bar) for the $\lambda_O = 0, t_d/t = 0.5$ and $U/t = 1.5$ case. One can observe that the Z_2 invariant is exactly integer-quantized to ± 1 [Fig. 6(a)]. Such integer quantization in finite-size system is due to the spatial inversion and particle-hole symmetries of the CKMH model. These two symmetries result in the special matrix structure of $G_\sigma(i\omega = 0, \boldsymbol{\kappa})$ in Eq. (22), which is sufficient to guarantee that the parities at TRIM points are exactly ± 1. As shown in Figs. 6(a), 6(b), and 6(c), for both $L = 6$ and $L = 12$, the λ_I-driven topological phase transition point is at $\lambda_I/t = 0.288 \sim 0.289$ from the drop in Z_2 invariant $(-1)^\nu$ and the jump in Chern number $C_\uparrow$. Across the topological phase transition, both single-particle gap close and the parity change all happen at $\boldsymbol{\Gamma}$ point. As for the Chern number $C_\uparrow$ from finite size $L = 6$ and $L = 12$ QMC calculation [Fig. 6(b) and 6(c)], they are still far from the ideal quantized result due to the finite-size effect, although the trend of convergence with increasing system size is present.

The calculation results of Chern number $C_\uparrow$ by the interpolation process for the λ_I-driven topological phase transition is presented in Figs. 6(b) and 6(c), from the QMC data in $L = 6$ and 12 systems. We can observe that the interpolation method can give good results of quantized integer for $C_\uparrow$. The non-monotonic behavior in $IL = 12, 24, 48$ close to the transition in Fig. 6(b) is due to the inappropriate τ cutoff in calculating Eq. (15), as mentioned in Sec. III C. This behavior is absent for large enough ILs. Through the interpolation method, a sharp topological phase transition from $C_s = 0$ to $C_s = +1$ can be clearly seen. Similarly, Z_2 invariant $(-1)^\nu$ and Chern number $C_\uparrow$ for the case of λ_I-driven topological phase transition with $\alpha = 1.8, U/t = 2$ are also calculated (shown in Appendix F).

V. CONCLUSION

To conclude, we provide a toolkit to calculate the topological invariants constructed from zero-frequency single-particle Green's function for interacting TIs. All the important numerical details are carefully documented, hence serves the purpose of demystifying the numerical evaluation of Z_2 invariant and spin Chern number for interacting TIs. Most importantly, we introduce an interpolation process to eliminate the finite-size effect on spin Chern number and obtain quantized topological invariants from finite-size QMC simulations, which renders the topological phases well defined.

To demonstrate the power of our calculation scheme, especially the interpolation process, both the topological phases and topological phase transitions in two interacting TI models, namely, the generalized Kane-Mele-Hubbard model and the cluster Kane-Mele-Hubbard model, are identified by numerical evaluation of topological invariants. The results show that the numerical scheme works well in capturing the topological phases and their phase transitions driven by one-body model parameter. The Z_2 invariants are already integer quantized by applying the symmetry properties of the studied system during data process. With the interpolation process, the integer-quantized spin Chern number is also achieved with QMC simulations in systems with very small size. Through these calculations of topological invariants, we can also determine the topological phase transition points accurately, at least more accurately than those from the gap extrapolations.

The present paper demonstrates that the numerical evaluation scheme, especially the interpolation process, of topological invariants for interacting TIs works well, in distinguishing topologically phases and identifying their phase transitions driven by the one-body model parameters. In paper II of this series, we shall apply the numerical evaluation scheme developed here to wider classes of models of interacting TIs, in which certain limitation of constructing topological invariants from single-particle Green's function is manifested in a very interesting manner, calling for more versatile technique to diagnose the interaction-driven topological phase transitions in interacting TIs.

ACKNOWLEDGMENTS

We thank Ning-Hua Tong, Lei Wang, Yi-Zhuang You, Cenke Xu, Liang Fu, and Xi Dai for inspiring discussions, and in particular we acknowledge Zhong Wang for helpful comments on the Green's function formalism and the manuscript. The numerical calculations were carried out at the Physical Laboratory of High Performance Computing in RUC, the Center for Quantum Simulation Sciences in the Institute of Physics, Chinese Academy of Sciences, as well as the National Supercomputer Center in Tianjin (TianHe-1A). Y.Y.H., H.Q.W., Z.Y.M. and Z.Y.L. acknowledge support from National Natural Science Foundation of China (Grant Nos. 11474356, 11190024, 11421092, and 11574359) and National Program for Basic Research of MOST of China (Grant No. 2011CBA00112). Z.Y.M. is also supported by the National Thousand-Young-Talents Program of China, and acknowledges the hospitality of the KITP at the University of California, Santa Barbara, where part of this work was completed.

APPENDIX A: DETAILED IMPLEMENTATION OF EQ. (4) FOR HONEYCOMB LATTICE

In this appendix, we present the numerical implementation of Eq. (4) on honeycomb lattice, provided that we have already obtained the zero-frequency single-particle Green's function data $G_\sigma(i\omega=0,\mathbf{k})$. The reason for having this discussion is that the primitive vectors for honeycomb lattice in real $(\mathbf{a}_1,\mathbf{a}_2)$ and momentum space $(\mathbf{b}_1,\mathbf{b}_2)$ [see Figs. 1(a), 1(b)] are not along the (x,y) or (k_x,k_y) direction of the Cartesian coordinate. Hence, both the integral over honeycomb lattice BZ and the derivatives over (k_x,k_y) in Eq. (4) can be Jacobian transformed from those on the honeycomb lattice BZ to that on a square lattice as

$$\begin{cases} q_u = k_x \\ q_v = \frac{k_x+\sqrt{3}k_y}{2} \end{cases} \qquad \begin{cases} 0 \leqslant q_u \leqslant \frac{2\pi}{\sqrt{3}a} \\ 0 \leqslant q_v \leqslant \frac{2\pi}{\sqrt{3}a} \end{cases} \qquad \Longrightarrow \qquad k_x = q_u \qquad k_y = \frac{-q_u+2q_v}{\sqrt{3}}. \tag{A1}$$

The transformed BZ is indeed a square one, and we can rewrite Eq. (4) by substituting Eq. (A1) as

$$\mathcal{C} = \frac{1}{2\pi i}\int_0^{2\pi/\sqrt{3}a} dq_u \int_0^{2\pi/\sqrt{3}a} dq_v \cdot \mathrm{Tr}\{Q(q_u,q_v)[\partial_{q_u}Q(q_u,q_v)\partial_{q_v}Q(q_u,q_v) - \partial_{q_v}Q(q_u,q_v)\partial_{q_u}Q(q_u,q_v)]\}, \tag{A2}$$

where $Q(q_u,q_v) = P(q_u,(-q_u+2q_v)/\sqrt{3})$ and $P(k_x,k_y)$ is the projection matrix defined in Eq. (5). Comparing Eq. (4) and Eq. (A2), one observes the Jacobian transformation does not change the form of the formula.

QMC simulates finite size system, so the integration and derivation in Eq. (A2) are discretized, we set $Q_{i,j} = Q(q_{u,i},q_{v,j})$ and $(q_{u,i},q_{v,j}) = (2i\pi/\sqrt{3}L_1a, 2j\pi/\sqrt{3}L_2a)$ with $i \in [0,L_1], j \in [0,L_2]$, then we have the expressions for finite difference as

$$\partial_{q_u}Q(q_u,q_v)|_{\mathbf{q}=(q_{u,i},q_{v,j})} = \frac{Q_{i+1,j}-Q_{i-1,j}}{2\delta_{q_u}} \qquad \partial_{q_v}Q(q_u,q_v)|_{\mathbf{q}=(q_{u,i},q_{v,j})} = \frac{Q_{i,j+1}-Q_{i,j+1}}{2\delta_{q_v}}, \tag{A3}$$

where $\delta_{q_u} = 2\pi/\sqrt{3}L_1a, \delta_{q_v} = 2\pi/\sqrt{3}L_2a$. Due to the periodic boundary condition, we have $Q_{0,j} = Q_{L_1,j}, Q_{L_1+1,j} = Q_{1,j}$ and $Q_{i,0} = Q_{i,L_2}, Q_{i,L_2+1} = Q_{i,1}$. Based on Eq. (A3), we arrive at the expression for the integrand in Eq. (A2) as

$$\begin{aligned} &\mathrm{Tr}\{Q(q_u,q_v)(\partial_{q_u}Q(q_u,q_v)\partial_{q_v}Q(q_u,q_v) - \partial_{q_v}Q(q_u,q_v)\partial_{q_u}Q(q_u,q_v))\} \\ &= \frac{1}{4\delta_{q_u}\delta_{q_v}}\mathrm{Tr}\{Q_{i,j}([Q_{i+1,j},Q_{i,j+1}] + [Q_{i,j+1},Q_{i-1,j}] + [Q_{i-1,j},Q_{i,j-1}] + [Q_{i,j-1},Q_{i+1,j}])\}. \end{aligned} \tag{A4}$$

Simultaneously, the integral over the square BZ in Eq. (A2) is changed into summation over discrete wave-vector points as

$$\int_{\mathbf{k}\in BZ} f(\mathbf{k})d^2\mathbf{k} = \frac{\Omega_{BZ}}{L_1L_2}\sum_{\mathbf{k}\in BZ} f(\mathbf{k}), \tag{A5}$$

where L_1L_2 is the number of unit cells for the finite size system, and $\Omega_{BZ} = 4\pi^2/3a$ is the volume of BZ. For a finite-size system, the result of the summation will deviate from the expected quantized integer, which is the finite-size effect we have seen in the main text, i.e., Figs. 3, 7, 6, and 8, but we have also seen that the summation results converge to the quantized integer with increasing system size. Combining Eqs. (A4) and (A5), we deduce the constant coefficient for Eq. (A2) as

$$\frac{1}{2\pi i}\cdot\frac{1}{4\delta_{q_u}\delta_{q_v}}\cdot\frac{\Omega_{BZ}}{N} = \frac{1}{2\pi i}\cdot\frac{3L_1L_2a^2}{16\pi^2}\cdot\frac{4\pi^2}{3L_1L_2a^2} = \frac{1}{8\pi i}. \tag{A6}$$

So finally, we can get the simplified expression of Eq. (A2) as

$$\mathcal{C} = \frac{1}{8\pi i}\sum_{i=1}^{L_1}\sum_{j=1}^{L_2} S(q_{u,i},q_{v,j})$$

$$S(q_{u,i},q_{v,j}) = \mathrm{Tr}\{Q_{i,j}([Q_{i+1,j},Q_{i,j+1}] + [Q_{i,j+1},Q_{i-1,j}] + [Q_{i-1,j},Q_{i,j-1}] + [Q_{i,j-1},Q_{i+1,j}])\}$$

$$(q_{u,i},q_{v,j}) = \left(\frac{2i\pi}{\sqrt{3}L_1 a},\frac{2j\pi}{\sqrt{3}L_2 a}\right) \qquad Q_{i,j} = Q(q_{u,i},q_{v,j}) \qquad Q(q_u,q_v) = P\left(q_u,\frac{-q_u+2q_v}{\sqrt{3}}\right). \tag{A7}$$

During the calculation, we only need to prepare the projection matrix $P(q_u,(-q_u+2q_v)/\sqrt{3})$ through the zero-frequency Green's function matrix obtained from QMC simulation. As Chern number should be an integer for a gapped system, we can only calculate the imaginary part of $S(q_{u,i},q_{v,j})$ in Eq. (A7).

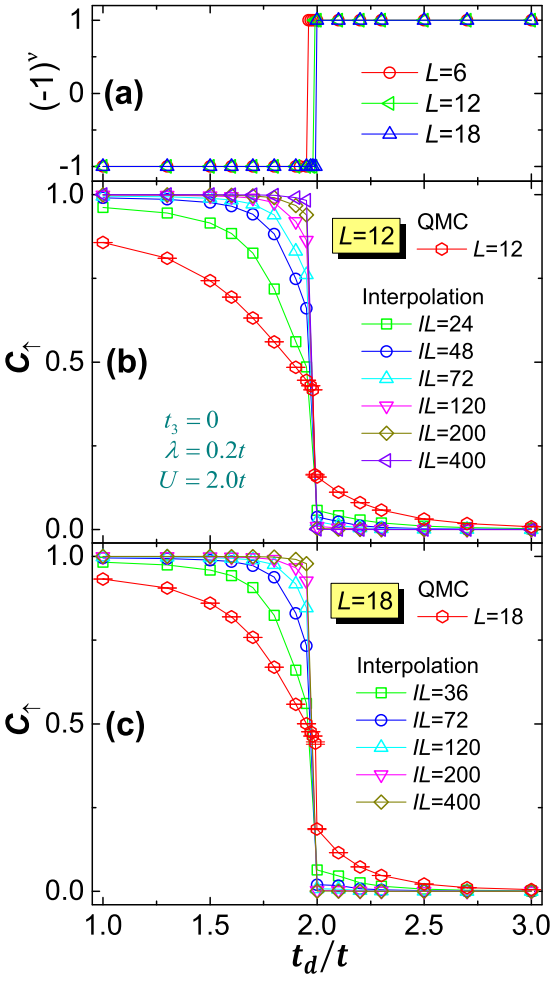

FIG. 7. (a) Z_2 invariant $(-1)^\nu$ and (b), (c) Chern number $C_\uparrow$ for the t_d-driven topological phase transition in the GKMH model with $t_3/t = 0, \lambda/t = 0.2$ and $U/t = 2.0$ from finite-size QMC simulation and interpolation process. (a) Z_2 invariant is integer quantized and there is a gradual shifting of the transition point from $t_d/t \approx 1.955$ in $L = 6$ system to $t_d/t \approx 1.995$ in the $L = 18$ system. (b) and (c), the finite drop in Chern number from finite-size QMC calculation with $L = 12$ and $L = 18$ (denoted by red open hexagon with error bar) can be observed clearly. The interpolation results of Chern number $C_\uparrow$, with the QMC data in $L = 12$ (b) and $L = 18$ (c) systems, are ideally quantized.

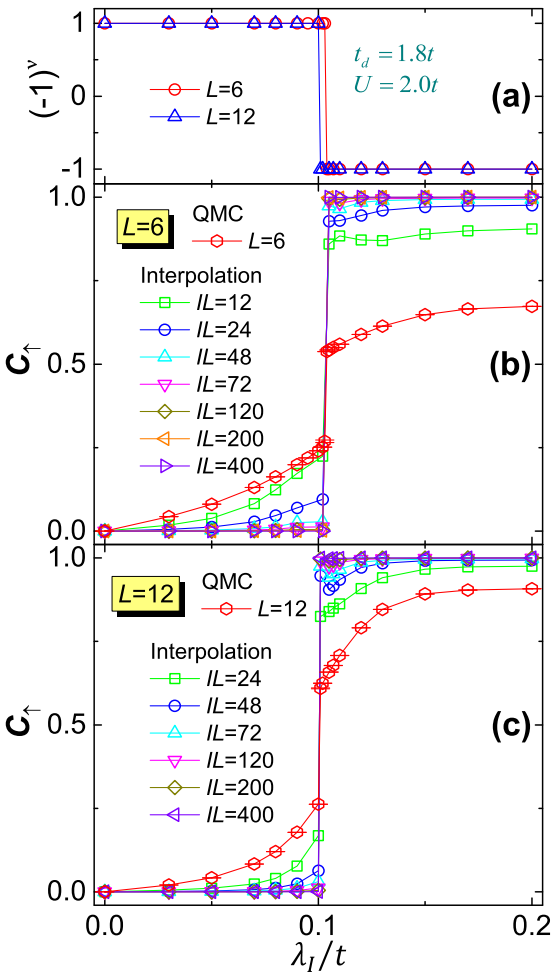

FIG. 8. (a) Z_2 invariant $(-1)^\nu$ and (b), (C) Chern number $C_\uparrow$ for the λ_I-driven topological phase transition in the CKMH model with $\alpha = 1.8$ and $U/t = 2.0$ from finite-size calculations by QMC (denoted by red open hexagon with error bar) and interpolation process. The drop of integer-valued Z_2 invariant and the jump of Chern number $C_\uparrow$ can be taken as signature of topological phase transition. In (b) and (c), with large IL in interpolation, the Chern number $C_\uparrow$ reaches its quantized value.

APPENDIX B: VALIDITY OF EQ. (10) AT ZERO TEMPERATURE

In this appendix, we validate the usage of Eq. (10) in obtaining $G(i\omega,\mathbf{k})$ data from $G(\tau,\mathbf{k})$ at zero temperature. Let's start with a review on some basic facts about Matsubara frequency Green's function at finite temperature. The Matsubara frequencies, $i\omega_n = i(2n+1)\pi/\beta, n \in Z$ for fermion systems and $i\omega_n = i2n\pi/\beta, n \in Z$ for boson systems, are actually the poles of the corresponding Fermi-Dirac and Bose-Einstein distribution function as

$$\begin{aligned} n_{FD}(\varepsilon) &= \frac{1}{e^{\beta\varepsilon}+1} \\ &= \frac{1}{2} + \frac{1}{\beta}\sum_{n=-\infty}^{+\infty}\frac{1}{i\omega_n-\varepsilon} \qquad \omega_n = \frac{(2n+1)\pi}{\beta} \\ n_{BE}(\varepsilon) &= \frac{1}{e^{\beta\varepsilon}-1} \\ &= -\frac{1}{2} - \frac{1}{\beta}\sum_{n=-\infty}^{+\infty}\frac{1}{i\omega_n-\varepsilon} \qquad \omega_n = \frac{2n\pi}{\beta}. \end{aligned} \tag{B1}$$

We can explicitly observe that for fermions the exact zero Matsubara frequency $i\omega = 0$ can only be physically reachable at zero temperature. Otherwise, the imaginary-time single-particle Green's function at finite temperature is defined as

$$\begin{aligned} G(\tau,\hat{A}\hat{B}) = -\langle T_\tau[\hat{A}(\tau)\hat{B}(0)]\rangle &= -\theta(\tau)\langle e^{\tau\hat{H}}\hat{A}e^{-\tau\hat{H}}\hat{B}\rangle \\ &\pm\theta(-\tau)\langle\hat{B}e^{\tau\hat{H}}\hat{A}e^{-\tau\hat{H}}\rangle, \end{aligned} \tag{B2}$$

where $+$ is for fermionic operators and $-$ is for bosonic operators, while $\hat{A}$ and $\hat{B}$ stands for single-particle fermionic or bosonic operators. According to this definition, one can simply prove the periodic and antiperiodic properties of $G(\tau,\hat{A}\hat{B})$ for fermionic and bosonic systems as

$$\begin{aligned} \text{Fermion:} G(\tau,\hat{A}\hat{B}) &= -G(\beta+\tau,\hat{A}\hat{B}) \\ \text{Boson:} G(\tau,\hat{A}\hat{B}) &= G(\beta+\tau,\hat{A}\hat{B}). \end{aligned} \tag{B3}$$

We can also write down the Lehmann representation of $G(\tau,\hat{A}\hat{B})$ for both fermionic and bosonic systems via expanding the expectation by all many-body eigenstates of the system as

$$\begin{aligned} G(\tau,\hat{A}\hat{B}) = \frac{1}{Z}\sum_{mn} e^{(E_m-E_n)\tau}&[-\theta(\tau)e^{-\beta E_m} \pm \theta(-\tau)e^{-\beta E_n}] \\ &\times\langle m|\hat{A}|n\rangle\langle n|\hat{B}|m\rangle. \end{aligned} \tag{B4}$$

For finite temperature case, the Fourier transformation between the imaginary-time Green's function $G(\tau,\hat{A}\hat{B})$ and the Matsubara frequency Green's function $G(i\omega_n,\hat{A}\hat{B})$

$$G(i\omega_n,\hat{A}\hat{B}) = \int_0^\beta G(\tau,\hat{A}\hat{B})e^{i\omega_n\tau}d\tau. \tag{B5}$$

So the Lehmann representation expression of $G(i\omega_n,\hat{A}\hat{B})$ is

$$\begin{aligned} G(i\omega_n,\hat{A}\hat{B}) &= \sum_{mn} D_{mn}\frac{\langle n|\hat{A}|m\rangle\langle m|\hat{B}|n\rangle}{i\omega_n-(E_m-E_n)} \\ D_{mn} &= \frac{\pm e^{-\beta E_m}+e^{-\beta E_n}}{Z}, \end{aligned} \tag{B6}$$

where the sign $\pm$ originates from the term $e^{i\omega_n\beta} = +1$ for bosons and $e^{i\omega_n\beta} = -1$ for fermions. The above formulas summarize the basic properties of Matsubara frequency Green's function.

At exact zero temperature, we have the Lehmann representation for $G(\tau,\mathbf{k})$ as

$$\begin{aligned} G(\tau,\hat{A}\hat{B}) = \sum_m [&-\theta(\tau)e^{(E_0-E_m)\tau}\langle 0|\hat{A}|m\rangle\langle m|\hat{B}|0\rangle \\ &\pm\theta(-\tau)e^{-(E_0-E_m)\tau}\langle m|\hat{A}|0\rangle\langle 0|\hat{B}|m\rangle]. \end{aligned} \tag{B7}$$

Taking $\beta\to+\infty$ limit in Eq. (B6), the Lehmann representation for $G(i\omega,\hat{A}\hat{B})$ at zero temperature can also be reached as

$$G(i\omega,\hat{A}\hat{B}) = \sum_m\left[\frac{\langle 0|\hat{A}|m\rangle\langle m|\hat{B}|0\rangle}{i\omega-(E_m-E_0)} \pm \frac{\langle m|\hat{A}|0\rangle\langle 0|\hat{B}|m\rangle}{i\omega+(E_m-E_0)}\right]. \tag{B8}$$

Now the problem is, at zero temperature, Fourier transformation in Eq. (B5) cannot transfer $G(\tau,\hat{A}\hat{B})$ in Eq. (B7) to $G(i\omega,\hat{A}\hat{B})$ in Eq. (B8), since Eq. (B8) cannot be obtained if one naively takes $\beta\to+\infty$ limit in Eq. (B5), which corresponds to integration domain $[0,+\infty]$. To solve this problem, we present a simple generalization of finite temperature Matsubara frequency Green's function formalism into the zero-temperature case, by altering the Fourier transformation in Eq. (B5) to the following one as

$$G(i\omega,\hat{A}\hat{B}) = \int_{-\infty}^{+\infty} G(\tau,\hat{A}\hat{B})e^{i\omega\tau}d\tau. \tag{B9}$$

With this new transformation, we can now obtain Eq. (B8) from Eq. (B7), at zero temperature. In practical QMC simulations, we do not take the integral in Eq. (B9) to $\pm\infty$, and instead we carry out a cutoff for τ in the integral as Eq. (15) in the main text. Nevertheless, Eq. (B9) validates the usage of Eq. (11) in the main text calculating $G(i\omega=0,\mathbf{k})$ from $G(\tau,\mathbf{k})$ matrix obtained from QMC simulations.

APPENDIX C: PROOF OF EQS. (12)–(14)

The definition of $[G_\sigma(\tau,\mathbf{k})]_{pq}$ with $p,q = 1,2,\ldots,m$ as orbitals for each spin sector in a unit cell, is

$$\begin{aligned} [G_\sigma(\tau,\mathbf{k})]_{pq} &= -\langle T_\tau[c_{\mathbf{k}p\sigma}(\tau)c^\dagger_{\mathbf{k}q\sigma}(0)]\rangle \\ &= -\frac{1}{N}\sum_{i,j=1}^{N} e^{-i\mathbf{k}\cdot(\mathbf{R}_i-\mathbf{R}_j)}\langle T_\tau[c_{ip\sigma}(\tau)c^\dagger_{jq\sigma}(0)]\rangle, \end{aligned} \tag{C1}$$

where $N = L^2$ is the number of unit cells. Then we have

$$[G_\sigma(\tau,\mathbf{k})]^\star_{qp} = -\frac{1}{N}\sum_{i,j=1}^{N} e^{i\mathbf{k}\cdot(\mathbf{R}_i-\mathbf{R}_j)}\langle T_\tau[c_{iq\sigma}(\tau)c^\dagger_{jp\sigma}(0)]\rangle^\star. \tag{C2}$$

For any operator, we have $\langle\phi|\hat{A}|\phi\rangle^\star = \langle\phi|\hat{A}^\dagger|\phi\rangle$, which means $\langle\hat{A}\rangle^\star = \langle\hat{A}^\dagger\rangle$. Based on this relation, we have

$$\langle T_\tau[c_{iq\sigma}(\tau)c^\dagger_{jp\sigma}(0)]\rangle^\star = \langle T_\tau[c_{jp\sigma}(\tau)c^\dagger_{iq\sigma}(0)]\rangle. \tag{C3}$$

Then we can prove

$$\begin{aligned}[G_\sigma(\tau,\mathbf{k})]^\star_{qp} &= -\frac{1}{N}\sum_{i,j=1}^{N} e^{i\mathbf{k}\cdot(\mathbf{R}_i-\mathbf{R}_j)}\langle T_\tau[c_{jp\sigma}(\tau)c^\dagger_{iq\sigma}(0)]\rangle \\ &= -\frac{1}{N}\sum_{i,j=1}^{N} e^{-i\mathbf{k}\cdot(\mathbf{R}_i-\mathbf{R}_j)}\langle T_\tau[c_{ip\sigma}(\tau)c^\dagger_{jq\sigma}(0)]\rangle \\ &= [G_\sigma(\tau,\mathbf{k})]_{pq}. \end{aligned} \tag{C4}$$

So the proof for Eq. (12) is complete.

For Eq. (13), the inversion operation $\hat{\mathcal{I}}$ (in each spin sector) transforms p sublattice to p'. For GKMH model, $\hat{\mathcal{I}}$ transfers A sublattice into B as $1 \leftrightarrow 2$, shown in Fig. 1(a), while it transfers $1 \leftrightarrow 4, 2 \leftrightarrow 5$ and $3 \leftrightarrow 6$ for the CKMH model, shown in Fig. 4. We assume the relation $p \leftrightarrow p'$ and $q \leftrightarrow q'$ under the spatial inversion symmetry operation for generally multiband systems. As the position vector should be inverse under $\hat{\mathcal{I}}$, i.e., $\mathbf{R}_i \to -\mathbf{R}_i$ we obtain the transformation for simple operators $c_{\mathbf{k}p\sigma}, c_{\mathbf{k}q\sigma}$ in reciprocal space as

$$\begin{aligned} c_{\mathbf{k}p\sigma} &= \frac{1}{\sqrt{N}}\sum_i e^{-i\mathbf{k}\cdot\mathbf{R}_i}c_{ip\sigma} \quad \to \\ \mathcal{I}c_{\mathbf{k}p\sigma}\mathcal{I}^{-1} &= \frac{1}{\sqrt{N}}\sum_i \mathcal{I}e^{-i\mathbf{k}\cdot\mathbf{R}_i}\mathcal{I}^{-1}\cdot\mathcal{I}^{-1}c_{ip\sigma}\mathcal{I}^{-1} \\ &= \frac{1}{\sqrt{N}}\sum_i e^{i\mathbf{k}\cdot\mathbf{R}_i}c_{ip'\sigma} = c_{-\mathbf{k}p'\sigma}. \end{aligned} \tag{C5}$$

Similarly, we have

$$\begin{aligned} \mathcal{I}c^\dagger_{\mathbf{k}p\sigma}\mathcal{I}^{-1} &= c^\dagger_{-\mathbf{k}p'\sigma} \\ \mathcal{I}c_{\mathbf{k}q\sigma}(\tau)\mathcal{I}^{-1} &= c_{-\mathbf{k}q'\sigma}(\tau), \\ \mathcal{I}c^\dagger_{\mathbf{k}q\sigma}(\tau)\mathcal{I}^{-1} &= c^\dagger_{-\mathbf{k}q'\sigma}(\tau). \end{aligned} \tag{C6}$$

So for the imaginary-time Green's function matrix, we have

$$\begin{aligned} \mathcal{I}[G_\sigma(\tau,\mathbf{k})]_{pq}\mathcal{I}^{-1} &= -\langle T_\tau[\mathcal{I}c_{\mathbf{k}p\sigma}(\tau)c^\dagger_{\mathbf{k}q\sigma}\mathcal{I}^{-1}]\rangle \\ &= -\langle T_\tau[\mathcal{I}c_{\mathbf{k}p\sigma}(\tau)\mathcal{I}^{-1}\mathcal{I}c^\dagger_{\mathbf{k}q\sigma}\mathcal{I}^{-1}]\rangle \\ &= -\langle c_{-\mathbf{k}p'\sigma}(\tau)c^\dagger_{-\mathbf{k}q'\sigma}\rangle \\ &= [G_\sigma(\tau,-\mathbf{k})]_{p'q'} \end{aligned} \tag{C7}$$

Due to the spatial inversion symmetry, the $G(\tau,\mathbf{k})$ matrix should be invariant under the inversion symmetry operation, from which we can get

$$[G_\sigma(\tau,\mathbf{k})]_{pq} = [G_\sigma(\tau,-\mathbf{k})]_{p'q'}. \tag{C8}$$

This is exactly Eq. (13).

Finally, we prove the relation Eq. (14). The standard definition for $[G_\sigma(\tau,\mathbf{k})]_{pq}$ is

$$\begin{aligned} [G_\sigma(\tau,\mathbf{k})]_{pq} &= -\langle T_\tau[c_{\mathbf{k}p\sigma}(\tau)c^\dagger_{\mathbf{k}q\sigma}(0)]\rangle = -\theta(\tau)\langle c_{\mathbf{k}p\sigma}(\tau)c^\dagger_{\mathbf{k}q\sigma}\rangle + \theta(-\tau)\langle c^\dagger_{\mathbf{k}q\sigma}c_{\mathbf{k}p\sigma}(\tau)\rangle \\ &= -\theta(\tau)\langle c_{\mathbf{k}p\sigma}c^\dagger_{\mathbf{k}q\sigma}(-\tau)\rangle + \theta(-\tau)\langle c^\dagger_{\mathbf{k}q\sigma}(-\tau)c_{\mathbf{k}p\sigma}\rangle \\ &= -\theta(\tau)\frac{1}{N}\sum_{i,j=1}^{N} e^{-i\mathbf{k}\cdot(\mathbf{R}_i-\mathbf{R}_j)}\langle c_{ip\sigma}c^\dagger_{jq\sigma}(-\tau)\rangle + \theta(-\tau)\frac{1}{N}\sum_{i,j=1}^{N} e^{-i\mathbf{k}\cdot(\mathbf{R}_i-\mathbf{R}_j)}\langle c^\dagger_{jq\sigma}(-\tau)c_{ip\sigma}\rangle, \end{aligned} \tag{C9}$$

where we have applied the the following relations

$$\langle c_{\mathbf{k}p\sigma}(\tau)c^\dagger_{\mathbf{k}q\sigma}\rangle = \langle c_{\mathbf{k}p\sigma}c^\dagger_{\mathbf{k}q\sigma}(-\tau)\rangle \qquad \langle c^\dagger_{\mathbf{k}q\sigma}c_{\mathbf{k}p\sigma}(\tau)\rangle = \langle c^\dagger_{\mathbf{k}q\sigma}(-\tau)c_{\mathbf{k}p\sigma}\rangle. \tag{C10}$$

Then we carry out the particle-hole transformation for $[G_\sigma(\tau,\mathbf{k})]_{pq}$ as $c_p \to \xi_p d^\dagger_p$ and $c_q \to \xi_q d^\dagger_q$, we have

$$\begin{aligned} \frac{1}{N}\sum_{i,j=1}^{N} e^{-i\mathbf{k}\cdot(\mathbf{R}_i-\mathbf{R}_j)}\langle c_{ip\sigma}c^\dagger_{jq\sigma}(-\tau)\rangle \quad\longrightarrow\quad & \frac{1}{N}\sum_{i,j=1}^{N} e^{-i\mathbf{k}\cdot(\mathbf{R}_i-\mathbf{R}_j)}\xi_p\xi_q\langle d^\dagger_{ip\sigma}d_{jq\sigma}(-\tau)\rangle \\ & = \xi_p\xi_q\langle d^\dagger_{-\mathbf{k}p\sigma}d_{-\mathbf{k}q\sigma}(-\tau)\rangle, \end{aligned} \tag{C11}$$

and the other term

$$\begin{aligned} \frac{1}{N}\sum_{i,j=1}^{N} e^{-i\mathbf{k}\cdot(\mathbf{R}_i-\mathbf{R}_j)}\langle c^\dagger_{jq\sigma}(-\tau)c_{ip\sigma}\rangle \quad\longrightarrow\quad & \frac{1}{N}\sum_{i,j=1}^{N} e^{-i\mathbf{k}\cdot(\mathbf{R}_i-\mathbf{R}_j)}\xi_p\xi_q\langle d_{jq\sigma}(-\tau)d^\dagger_{ip\sigma}\rangle \\ & = \xi_p\xi_q\langle d_{-\mathbf{k}q\sigma}(-\tau)d^\dagger_{-\mathbf{k}p\sigma}\rangle. \end{aligned} \tag{C12}$$

Combining the results of these two terms, under the particle-hole transformation, $[G_\sigma(\tau,\mathbf{k})]_{pq}$ changes to

$$[G_\sigma(\tau,\mathbf{k})]_{pq} \quad\longrightarrow\quad -\theta(\tau)\xi_p\xi_q\langle d^\dagger_{-\mathbf{k}p\sigma}d_{-\mathbf{k}q\sigma}(-\tau)\rangle + \theta(-\tau)\xi_p\xi_q\langle d_{-\mathbf{k}q\sigma}(-\tau)d^\dagger_{-\mathbf{k}p\sigma}\rangle. \tag{C13}$$

On the other hand, we can write down $[G_\sigma(-\tau,-\mathbf{k})]_{qp}$ according to original definition in Eq. (C9)

$$[G_\sigma(-\tau,-\mathbf{k})]_{qp} = -\theta(-\tau)\langle c_{-\mathbf{k}q\sigma}(-\tau)c^\dagger_{-\mathbf{k}p\sigma}\rangle + \theta(\tau)\langle c^\dagger_{-\mathbf{k}p\sigma}c_{-\mathbf{k}q\sigma}(-\tau)\rangle. \tag{C14}$$

Comparing Eqs. (C13) and (C14), and considering that the particle-hole symmetry is preserved, we arrive at

$$[G_\sigma(\tau,\mathbf{k})]_{pq} = -\xi_p\xi_q[G_\sigma(-\tau,-\mathbf{k})]_{qp}, \tag{C15}$$

which is Eq. (14) in the main text.

APPENDIX D: CONNECTION BETWEEN THE INTERPOLATION PROCESS IN SEC. III D AND PERIODIZATION IN CDMFT

In Sec. III D of the main text, we proposed an interpolation process for $G_\sigma(i\omega=0,\mathbf{k})$ based on two steps of discrete Fourier transformations. Actually, the process, especially the last step as Eq. (16), is inspired by the similar implementation in CDMFT, which is dubbed periodization. However, there are still some differences between the one we applied in this paper and that in CDMFT framework. In this section, we discuss these differences.

CDMFT simulates a correlated system within a cluster (with some other noninteracting bath energy levels) and open boundary condition is applied for the finite-size cluster. To recover the translational symmetry broken by the open boundary condition, a periodization process [43–46] is applied to construct the Green's function and self-energy with arbitrary momentum resolution. The periodization process is generally realized by

$$Q^L(i\omega_n,\mathbf{k}) = \frac{1}{N_c}\sum_{i,j=1}^{N_c} Q^C_{ij}(i\omega_n)e^{i\mathbf{k}\cdot(\mathbf{r}_i-\mathbf{r}_j)}, \tag{D1}$$

where N_c is the size of cluster, $Q^C(i\omega_n)$ is the quantity calculated on the cluster and $Q^L(\mathbf{k},i\omega_n)$ is the periodization result with arbitrary $\mathbf{k}$ point in BZ. In CDMFT, generally one can choose $Q^C(i\omega_n)$ to be $M^C(i\omega_n)$ and $\Sigma^C(i\omega_n)$, where $M^C(i\omega_n) = [i\omega_n + \mu - \Sigma^C(i\omega_n)]^{-1}$ is the cluster cumulant and $\Sigma^C(i\omega_n)$ is the cluster self-energy. Naively thinking, directly substituting $G^C(i\omega_n)$ into Eq. (D1) seems to be the simplest way, since matrix inverse operations are needed during numerical calculations if $Q^C(i\omega_n)$ is chosen to be $M^C(i\omega_n)$ and $\Sigma^C(i\omega_n)$ instead. However, due to the breaking of lattice translational symmetry, the simple G periodization can generate artificial results and another more complicated version of G periodization instead of Eq. (D1) should be applied to obtain reasonable results [45].

For our purpose of calculating spin Chern number in QMC, nevertheless, we can apply the G periodization method simply via Eq. (D1) by choosing $Q^C(i\omega_n)$ to be $G^C(i\omega_n)$ [the Green's function $G_{\sigma,ij}(i\omega=0)$ for $L\times L$ system in Eq. (16)]. Since the finite size Green's function $G(i\omega=0,\mathbf{k})$ or $G_{\sigma,ij}(i\omega=0)$ for $L\times L$ system obtained from QMC simulation actually respects the periodic boundary condition, this is different from the periodization in CDMFT [45] and guarantees our interpolation of Green's function to arbitrary $\mathbf{k}$ point in BZ gives rise to smooth curves.

APPENDIX E: DERIVATION OF EQS. (21) AND (22)

For the CKMH model, the spatial inversion operators as $1\leftrightarrow 4, 2\leftrightarrow 5$ and $3\leftrightarrow 6$ among the six sublattices. One can show that spatial inversion symmetry result in the following properties of $G_\sigma(\tau,\mathbf{k})$ matrix, according to Eq. (13).

$$\begin{aligned}
&[G_\sigma(\tau,\mathbf{k})]_{11} = [G_\sigma(\tau,-\mathbf{k})]_{44} \quad [G_\sigma(\tau,\mathbf{k})]_{12} = [G_\sigma(\tau,-\mathbf{k})]_{45} \quad [G_\sigma(\tau,\mathbf{k})]_{13} = [G_\sigma(\tau,-\mathbf{k})]_{46}\\
&[G_\sigma(\tau,\mathbf{k})]_{14} = [G_\sigma(\tau,-\mathbf{k})]_{41} \quad [G_\sigma(\tau,\mathbf{k})]_{15} = [G_\sigma(\tau,-\mathbf{k})]_{42} \quad [G_\sigma(\tau,\mathbf{k})]_{16} = [G_\sigma(\tau,-\mathbf{k})]_{43}\\
&[G_\sigma(\tau,\mathbf{k})]_{22} = [G_\sigma(\tau,-\mathbf{k})]_{55} \quad [G_\sigma(\tau,\mathbf{k})]_{23} = [G_\sigma(\tau,-\mathbf{k})]_{56} \quad [G_\sigma(\tau,\mathbf{k})]_{24} = [G_\sigma(\tau,-\mathbf{k})]_{51}\\
&[G_\sigma(\tau,\mathbf{k})]_{25} = [G_\sigma(\tau,-\mathbf{k})]_{52} \quad [G_\sigma(\tau,\mathbf{k})]_{26} = [G_\sigma(\tau,-\mathbf{k})]_{53}\\
&[G_\sigma(\tau,\mathbf{k})]_{33} = [G_\sigma(\tau,-\mathbf{k})]_{66} \quad [G_\sigma(\tau,\mathbf{k})]_{34} = [G_\sigma(\tau,-\mathbf{k})]_{61} \quad [G_\sigma(\tau,\mathbf{k})]_{35} = [G_\sigma(\tau,-\mathbf{k})]_{62}\\
&[G_\sigma(\tau,\mathbf{k})]_{36} = [G_\sigma(\tau,-\mathbf{k})]_{63}\\
&[G_\sigma(\tau,\mathbf{k})]_{44} = [G_\sigma(\tau,-\mathbf{k})]_{11} \quad [G_\sigma(\tau,\mathbf{k})]_{45} = [G_\sigma(\tau,-\mathbf{k})]_{12} \quad [G_\sigma(\tau,\mathbf{k})]_{46} = [G_\sigma(\tau,-\mathbf{k})]_{13}\\
&[G_\sigma(\tau,\mathbf{k})]_{55} = [G_\sigma(\tau,-\mathbf{k})]_{22} \quad [G_\sigma(\tau,\mathbf{k})]_{56} = [G_\sigma(\tau,-\mathbf{k})]_{23}\\
&[G_\sigma(\tau,\mathbf{k})]_{66} = [G_\sigma(\tau,-\mathbf{k})]_{33}
\end{aligned} \tag{E1}$$

The particle-hole operators with $\xi_1=+1,\xi_2=-1,\xi_3=+1,\xi_4=-1,\xi_5=+1,\xi_6=-1$, then according to Eq. (14), we have the following properties for $[G_\sigma(\tau,\mathbf{k})]_{1q}, q=1,2,3,4,5,6$ as

$$\begin{aligned}
&[G_\sigma(\tau,-\mathbf{k})]_{44} = -[G_\sigma(-\tau,\mathbf{k})]_{44} \quad [G_\sigma(\tau,-\mathbf{k})]_{45} = +[G_\sigma(-\tau,\mathbf{k})]_{54} \quad [G_\sigma(\tau,-\mathbf{k})]_{46} = -[G_\sigma(-\tau,\mathbf{k})]_{64}\\
&[G_\sigma(\tau,-\mathbf{k})]_{41} = +[G_\sigma(-\tau,\mathbf{k})]_{14} \quad [G_\sigma(\tau,-\mathbf{k})]_{42} = -[G_\sigma(-\tau,\mathbf{k})]_{24} \quad [G_\sigma(\tau,-\mathbf{k})]_{43} = +[G_\sigma(-\tau,\mathbf{k})]_{34}.
\end{aligned} \tag{E2}$$

With the condition of Hermitian matrix of $G_\sigma(\tau,\mathbf{k})$ in Eq. (12), we have $[G_\sigma(-\tau,\mathbf{k})]_{54} = [G_\sigma(-\tau,\mathbf{k})]^\star_{45}$,$[G_\sigma(-\tau,\mathbf{k})]_{64} = [G_\sigma(-\tau,\mathbf{k})]^\star_{46}$. With Eqs. (E1) and (E2), we have

$$\begin{aligned}
&[G_\sigma(\tau,\mathbf{k})]_{11} = -[G_\sigma(-\tau,\mathbf{k})]_{44} \qquad [G_\sigma(\tau,\mathbf{k})]_{12} = +[G_\sigma(-\tau,\mathbf{k})]^\star_{45} \qquad [G_\sigma(\tau,\mathbf{k})]_{13} = -[G_\sigma(-\tau,\mathbf{k})]^\star_{46} \\
&[G_\sigma(\tau,\mathbf{k})]_{14} = +[G_\sigma(-\tau,\mathbf{k})]_{14} \qquad [G_\sigma(\tau,\mathbf{k})]_{15} = -[G_\sigma(-\tau,\mathbf{k})]_{24} \qquad [G_\sigma(\tau,\mathbf{k})]_{16} = +[G_\sigma(-\tau,\mathbf{k})]_{34}.
\end{aligned} \tag{E3}$$

Similarly, for $[G_\sigma(\tau,\mathbf{k})]_{2q}$,$q = 2,3,4,5,6$ from the particle-hole symmetry, we have

$$\begin{aligned}
&[G_\sigma(\tau,-\mathbf{k})]_{55} = -[G_\sigma(-\tau,\mathbf{k})]_{55} \qquad [G_\sigma(\tau,-\mathbf{k})]_{56} = +[G_\sigma(-\tau,\mathbf{k})]_{65} \qquad [G_\sigma(\tau,-\mathbf{k})]_{51} = -[G_\sigma(-\tau,\mathbf{k})]_{15} \\
&[G_\sigma(\tau,-\mathbf{k})]_{52} = +[G_\sigma(-\tau,\mathbf{k})]_{25} \qquad [G_\sigma(\tau,-\mathbf{k})]_{53} = -[G_\sigma(-\tau,\mathbf{k})]_{35}.
\end{aligned} \tag{E4}$$

With $[G_\sigma(-\tau,\mathbf{k})]_{65} = [G_\sigma(-\tau,\mathbf{k})]^\star_{56}$ and combining Eqs. (E1) and (E4), we also have

$$\begin{aligned}
&[G_\sigma(\tau,\mathbf{k})]_{22} = -[G_\sigma(-\tau,\mathbf{k})]_{55} \qquad [G_\sigma(\tau,\mathbf{k})]_{23} = +[G_\sigma(-\tau,\mathbf{k})]^\star_{56} \qquad [G_\sigma(\tau,\mathbf{k})]_{24} = -[G_\sigma(-\tau,\mathbf{k})]_{15} \\
&[G_\sigma(\tau,\mathbf{k})]_{25} = +[G_\sigma(-\tau,\mathbf{k})]_{25} \qquad [G_\sigma(\tau,\mathbf{k})]_{26} = -[G_\sigma(-\tau,\mathbf{k})]_{35}.
\end{aligned} \tag{E5}$$

For $[G_\sigma(\tau,\mathbf{k})]_{3q}$,$q = 3,4,5,6$ from the particle-hole symmetry, we have

$$\begin{aligned}
&[G_\sigma(\tau,-\mathbf{k})]_{66} = -[G_\sigma(-\tau,\mathbf{k})]_{66} \qquad [G_\sigma(\tau,-\mathbf{k})]_{61} = +[G_\sigma(-\tau,\mathbf{k})]_{16} \qquad [G_\sigma(\tau,-\mathbf{k})]_{62} = -[G_\sigma(-\tau,\mathbf{k})]_{26} \\
&[G_\sigma(\tau,-\mathbf{k})]_{63} = +[G_\sigma(-\tau,\mathbf{k})]_{36}.
\end{aligned} \tag{E6}$$

Combining Eq. (E1) and Eq. (E6), we also have

$$\begin{aligned}
&[G_\sigma(\tau,\mathbf{k})]_{33} = -[G_\sigma(-\tau,\mathbf{k})]_{66} \qquad [G_\sigma(\tau,\mathbf{k})]_{34} = +[G_\sigma(-\tau,\mathbf{k})]_{16} \qquad [G_\sigma(\tau,\mathbf{k})]_{35} = -[G_\sigma(-\tau,\mathbf{k})]_{26} \\
&[G_\sigma(\tau,\mathbf{k})]_{36} = +[G_\sigma(-\tau,\mathbf{k})]_{36}.
\end{aligned} \tag{E7}$$

For $[G_\sigma(\tau,\mathbf{k})]_{4q}$,$q = 4,5,6$ from the particle-hole symmetry, we have

$$[G_\sigma(\tau,-\mathbf{k})]_{11} = -[G_\sigma(-\tau,\mathbf{k})]_{11} \qquad [G_\sigma(\tau,-\mathbf{k})]_{12} = +[G_\sigma(-\tau,\mathbf{k})]_{21} \qquad [G_\sigma(\tau,-\mathbf{k})]_{13} = -[G_\sigma(-\tau,\mathbf{k})]_{31} \tag{E8}$$

With $[G_\sigma(-\tau,\mathbf{k})]_{21} = [G_\sigma(-\tau,\mathbf{k})]^\star_{12}$,$[G_\sigma(-\tau,\mathbf{k})]_{31} = [G_\sigma(-\tau,\mathbf{k})]^\star_{13}$ and combining Eqs. (E1) and (E8), we also have

$$[G_\sigma(\tau,\mathbf{k})]_{44} = -[G_\sigma(-\tau,\mathbf{k})]_{11} \qquad [G_\sigma(\tau,\mathbf{k})]_{45} = +[G_\sigma(-\tau,\mathbf{k})]^\star_{12} \qquad [G_\sigma(\tau,\mathbf{k})]_{46} = -[G_\sigma(-\tau,\mathbf{k})]^\star_{13} \tag{E9}$$

For $[G_\sigma(\tau,\mathbf{k})]_{5q}$,$q = 5,6$ from the particle-hole symmetry, we have

$$[G_\sigma(\tau,-\mathbf{k})]_{22} = -[G_\sigma(-\tau,\mathbf{k})]_{22} \qquad [G_\sigma(\tau,-\mathbf{k})]_{23} = +[G_\sigma(-\tau,\mathbf{k})]_{32}. \tag{E10}$$

With $[G_\sigma(-\tau,\mathbf{k})]_{32} = [G_\sigma(-\tau,\mathbf{k})]^\star_{23}$ and combining Eqs. (E1) and (E10), we also have

$$[G_\sigma(\tau,\mathbf{k})]_{55} = -[G_\sigma(-\tau,\mathbf{k})]_{22} \qquad [G_\sigma(\tau,\mathbf{k})]_{56} = +[G_\sigma(-\tau,\mathbf{k})]^\star_{23}. \tag{E11}$$

For $[G_\sigma(\tau,\mathbf{k})]_{66}$ from the particle-hole symmetry, we have

$$[G_\sigma(\tau,-\mathbf{k})]_{33} = -[G_\sigma(-\tau,\mathbf{k})]_{33}. \tag{E12}$$

Combining Eqs. (E1) and (E12), we also have

$$[G_\sigma(\tau,\mathbf{k})]_{66} = -[G_\sigma(-\tau,\mathbf{k})]_{33}. \tag{E13}$$

To calculate the $G_\sigma(i\omega = 0,\mathbf{k})$ matrix, we need to apply the Fourier transformation as

$$G_\sigma(i\omega = 0,\mathbf{k}) = \int_{-\infty}^{+\infty} G_\sigma(\tau,\mathbf{k})d\tau. \tag{E14}$$

Then by Eq. (E14), we can show that there are actually only 12 independent matrix elements in $G_\sigma(i\omega = 0,\mathbf{k})$ matrix for CKMH model, which we need to calculate, combining Eqs. (E3), (E5), (E7), (E9), (E11), and (E13). For the diagonal matrix elements of $G_\sigma(i\omega = 0,\mathbf{k})$ matrix, we have three independent diagonal elements as

$$\begin{aligned}
A_1 &= [G_\sigma(i\omega = 0,\mathbf{k})]_{11} = \int_{-\infty}^{+\infty} [G_\sigma(\tau,\mathbf{k})]_{11}d\tau = \int_0^{+\infty} \{[G_\sigma(\tau,\mathbf{k})]_{11} - [G_\sigma(\tau,\mathbf{k})]_{44}\}d\tau = -[G_\sigma(i\omega = 0,\mathbf{k})]_{44} \\
A_2 &= [G_\sigma(i\omega = 0,\mathbf{k})]_{22} = \int_{-\infty}^{+\infty} [G_\sigma(\tau,\mathbf{k})]_{22}d\tau = \int_0^{+\infty} \{[G_\sigma(\tau,\mathbf{k})]_{22} - [G_\sigma(\tau,\mathbf{k})]_{55}\}d\tau = -[G_\sigma(i\omega = 0,\mathbf{k})]_{55} \\
A_3 &= [G_\sigma(i\omega = 0,\mathbf{k})]_{33} = \int_{-\infty}^{+\infty} [G_\sigma(\tau,\mathbf{k})]_{33}d\tau = \int_0^{+\infty} \{[G_\sigma(\tau,\mathbf{k})]_{33} - [G_\sigma(\tau,\mathbf{k})]_{66}\}d\tau = -[G_\sigma(i\omega = 0,\mathbf{k})]_{66}
\end{aligned} \tag{E15}$$

For the off-diagonal matrix elements, we can determine that there are only nine independent matrix off-diagonal elements in $G_\sigma(i\omega=0,\mathbf{k})$ matrix as

$$
\begin{aligned}
A_4 &= [G_\sigma(i\omega=0,\mathbf{k})]_{12} = \int_{-\infty}^{+\infty}[G_\sigma(\tau,\mathbf{k})]_{12}d\tau = \int_0^{+\infty}\{[G_\sigma(\tau,\mathbf{k})]_{12}+[G_\sigma(\tau,\mathbf{k})]^\star_{45}\}d\tau = +[G_\sigma(i\omega=0,\mathbf{k})]^\star_{45}\\
A_5 &= [G_\sigma(i\omega=0,\mathbf{k})]_{13} = \int_{-\infty}^{+\infty}[G_\sigma(\tau,\mathbf{k})]_{13}d\tau = \int_0^{+\infty}\{[G_\sigma(\tau,\mathbf{k})]_{13}-[G_\sigma(\tau,\mathbf{k})]^\star_{46}\}d\tau = -[G_\sigma(i\omega=0,\mathbf{k})]^\star_{46}\\
A_6 &= [G_\sigma(i\omega=0,\mathbf{k})]_{14} = \int_{-\infty}^{+\infty}[G_\sigma(\tau,\mathbf{k})]_{14}d\tau = 2\int_0^{+\infty}[G_\sigma(\tau,\mathbf{k})]_{14}d\tau\\
A_7 &= [G_\sigma(i\omega=0,\mathbf{k})]_{15} = \int_{-\infty}^{+\infty}[G_\sigma(\tau,\mathbf{k})]_{15}d\tau = \int_0^{+\infty}\{[G_\sigma(\tau,\mathbf{k})]_{15}-[G_\sigma(\tau,\mathbf{k})]_{24}\}d\tau = -[G_\sigma(i\omega=0,\mathbf{k})]_{24}\\
A_8 &= [G_\sigma(i\omega=0,\mathbf{k})]_{16} = \int_{-\infty}^{+\infty}[G_\sigma(\tau,\mathbf{k})]_{16}d\tau = \int_0^{+\infty}\{[G_\sigma(\tau,\mathbf{k})]_{16}+[G_\sigma(\tau,\mathbf{k})]_{34}\}d\tau = +[G_\sigma(i\omega=0,\mathbf{k})]_{34}\\
A_9 &= [G_\sigma(i\omega=0,\mathbf{k})]_{23} = \int_{-\infty}^{+\infty}[G_\sigma(\tau,\mathbf{k})]_{23}d\tau = \int_0^{+\infty}\{[G_\sigma(\tau,\mathbf{k})]_{23}+[G_\sigma(\tau,\mathbf{k})]^\star_{56}\}d\tau = +[G_\sigma(i\omega=0,\mathbf{k})]^\star_{56}\\
A_{10} &= [G_\sigma(i\omega=0,\mathbf{k})]_{25} = \int_{-\infty}^{+\infty}[G_\sigma(\tau,\mathbf{k})]_{25}d\tau = 2\int_0^{+\infty}[G_\sigma(\tau,\mathbf{k})]_{25}d\tau\\
A_{11} &= [G_\sigma(i\omega=0,\mathbf{k})]_{26} = \int_{-\infty}^{+\infty}[G_\sigma(\tau,\mathbf{k})]_{26}d\tau = \int_0^{+\infty}\{[G_\sigma(\tau,\mathbf{k})]_{26}-[G_\sigma(\tau,\mathbf{k})]_{35}\}d\tau = -[G_\sigma(i\omega=0,\mathbf{k})]_{35}\\
A_{12} &= [G_\sigma(i\omega=0,\mathbf{k})]_{36} = \int_{-\infty}^{+\infty}[G_\sigma(\tau,\mathbf{k})]_{36}d\tau = 2\int_0^{+\infty}[G_\sigma(\tau,\mathbf{k})]_{36}d\tau
\end{aligned}
\tag{E16}
$$

Then taking the τ cutoff θ and transforming the integral to summation over discrete τ, we can get the following matrix structure of $G_\sigma(i\omega=0,\mathbf{k})$ matrix as

$$
G_\sigma(i\omega=0,\mathbf{k}) = \begin{pmatrix}
A_1 & A_4 & A_5 & A_6 & A_7 & A_8\\
A_4^\star & A_2 & A_9 & -A_7 & A_{10} & A_{11}\\
A_5^\star & A_9^\star & A_3 & A_8 & -A_{11} & A_{12}\\
A_6^\star & -A_7^\star & A_8^\star & -A_1 & A_4^\star & -A_5^\star\\
A_7^\star & A_{10}^\star & -A_{11}^\star & A_4 & -A_2 & A_9^\star\\
A_8^\star & A_{11}^\star & A_{12}^\star & -A_5 & A_9 & -A_3
\end{pmatrix}.
\tag{E17}
$$

As for the Z_2 invariant for CKMH model, we only need to obtain the $G_\sigma(i\omega=0,\boldsymbol{\kappa})$ data at four TRIM points as $\boldsymbol{\kappa}=\boldsymbol{\Gamma},\mathbf{M}_1,\mathbf{M}_2,\mathbf{M}_3$. From the symmetry properties in Eq. (E1), we can obtain that for the TRIM points, we have

$$
\begin{aligned}
&[G_\sigma(\tau,\boldsymbol{\kappa})]_{11}=[G_\sigma(\tau,\boldsymbol{\kappa})]_{44} \quad [G_\sigma(\tau,\boldsymbol{\kappa})]_{12}=[G_\sigma(\tau,\boldsymbol{\kappa})]_{45} \quad [G_\sigma(\tau,\boldsymbol{\kappa})]_{13}=[G_\sigma(\tau,\boldsymbol{\kappa})]_{46}\\
&[G_\sigma(\tau,\boldsymbol{\kappa})]_{14}=[G_\sigma(\tau,\boldsymbol{\kappa})]_{41} \quad [G_\sigma(\tau,\boldsymbol{\kappa})]_{15}=[G_\sigma(\tau,\boldsymbol{\kappa})]_{42} \quad [G_\sigma(\tau,\boldsymbol{\kappa})]_{16}=[G_\sigma(\tau,\boldsymbol{\kappa})]_{43}\\
&[G_\sigma(\tau,\boldsymbol{\kappa})]_{22}=[G_\sigma(\tau,\boldsymbol{\kappa})]_{55} \quad [G_\sigma(\tau,\boldsymbol{\kappa})]_{23}=[G_\sigma(\tau,\boldsymbol{\kappa})]_{56} \quad [G_\sigma(\tau,\boldsymbol{\kappa})]_{24}=[G_\sigma(\tau,\boldsymbol{\kappa})]_{51}\\
&[G_\sigma(\tau,\boldsymbol{\kappa})]_{25}=[G_\sigma(\tau,\boldsymbol{\kappa})]_{52} \quad [G_\sigma(\tau,\boldsymbol{\kappa})]_{26}=[G_\sigma(\tau,\boldsymbol{\kappa})]_{53}\\
&[G_\sigma(\tau,\boldsymbol{\kappa})]_{33}=[G_\sigma(\tau,\boldsymbol{\kappa})]_{66} \quad [G_\sigma(\tau,\boldsymbol{\kappa})]_{34}=[G_\sigma(\tau,\boldsymbol{\kappa})]_{61} \quad [G_\sigma(\tau,\boldsymbol{\kappa})]_{35}=[G_\sigma(\tau,\boldsymbol{\kappa})]_{62}\\
&[G_\sigma(\tau,\boldsymbol{\kappa})]_{36}=[G_\sigma(\tau,\boldsymbol{\kappa})]_{63}\\
&[G_\sigma(\tau,\boldsymbol{\kappa})]_{44}=[G_\sigma(\tau,\boldsymbol{\kappa})]_{11} \quad [G_\sigma(\tau,\boldsymbol{\kappa})]_{45}=[G_\sigma(\tau,\boldsymbol{\kappa})]_{12} \quad [G_\sigma(\tau,\boldsymbol{\kappa})]_{46}=[G_\sigma(\tau,\boldsymbol{\kappa})]_{13}\\
&[G_\sigma(\tau,\boldsymbol{\kappa})]_{55}=[G_\sigma(\tau,\boldsymbol{\kappa})]_{22} \quad [G_\sigma(\tau,\boldsymbol{\kappa})]_{56}=[G_\sigma(\tau,\boldsymbol{\kappa})]_{23}\\
&[G_\sigma(\tau,\boldsymbol{\kappa})]_{66}=[G_\sigma(\tau,\boldsymbol{\kappa})]_{33}.
\end{aligned}
\tag{E18}
$$

Then we can determine that at TRIM points, we have $A_1=A_2=A_3=0$ and $[G_\sigma(\tau,\boldsymbol{\kappa})]_{14}$,$[G_\sigma(\tau,\boldsymbol{\kappa})]_{25}$ and $[G_\sigma(\tau,\boldsymbol{\kappa})]_{36}$ are all real numbers. From these relations, we have $B_6=A_6, B_{10}=A_{10}$ and $B_{12}=A_{12}$, and they are all real numbers as well. For other elements, we have

$$
\begin{aligned}
A_4 &= [G_\sigma(i\omega=0,\boldsymbol{\kappa})]_{12} = \int_{-\infty}^{+\infty}[G_\sigma(\tau,\boldsymbol{\kappa})]_{12}d\tau = \int_0^{+\infty}\{[G_\sigma(\tau,\boldsymbol{\kappa})]_{12}+[G_\sigma(\tau,\boldsymbol{\kappa})]^\star_{12}\}d\tau = B_4\\
A_5 &= [G_\sigma(i\omega=0,\boldsymbol{\kappa})]_{13} = \int_{-\infty}^{+\infty}[G_\sigma(\tau,\boldsymbol{\kappa})]_{13}d\tau = \int_0^{+\infty}\{[G_\sigma(\tau,\boldsymbol{\kappa})]_{13}-[G_\sigma(\tau,\boldsymbol{\kappa})]^\star_{13}\}d\tau = iB_5
\end{aligned}
$$

$$A_6 = [G_\sigma(i\omega = 0,\boldsymbol{\kappa})]_{14} = \int_{-\infty}^{+\infty} [G_\sigma(\tau,\boldsymbol{\kappa})]_{14} d\tau = 2\int_0^{+\infty} [G_\sigma(\tau,\boldsymbol{\kappa})]_{14} d\tau = B_6$$

$$A_7 = [G_\sigma(i\omega = 0,\boldsymbol{\kappa})]_{15} = \int_{-\infty}^{+\infty} [G_\sigma(\tau,\boldsymbol{\kappa})]_{15} d\tau = \int_0^{+\infty} \{[G_\sigma(\tau,\boldsymbol{\kappa})]_{15} - [G_\sigma(\tau,\boldsymbol{\kappa})]^\star_{15}\} d\tau = iB_7$$

$$A_8 = [G_\sigma(i\omega = 0,\boldsymbol{\kappa})]_{16} = \int_{-\infty}^{+\infty} [G_\sigma(\tau,\boldsymbol{\kappa})]_{16} d\tau = \int_0^{+\infty} \{[G_\sigma(\tau,\boldsymbol{\kappa})]_{16} + [G_\sigma(\tau,\boldsymbol{\kappa})]^\star_{16}\} d\tau = B_8$$

$$A_9 = [G_\sigma(i\omega = 0,\boldsymbol{\kappa})]_{23} = \int_{-\infty}^{+\infty} [G_\sigma(\tau,\boldsymbol{\kappa})]_{23} d\tau = \int_0^{+\infty} \{[G_\sigma(\tau,\boldsymbol{\kappa})]_{23} + [G_\sigma(\tau,\boldsymbol{\kappa})]^\star_{23}\} d\tau = B_9$$

$$A_{10} = [G_\sigma(i\omega = 0,\boldsymbol{\kappa})]_{25} = \int_{-\infty}^{+\infty} [G_\sigma(\tau,\boldsymbol{\kappa})]_{25} d\tau = 2\int_0^{+\infty} [G_\sigma(\tau,\boldsymbol{\kappa})]_{25} d\tau = B_{10}$$

$$A_{11} = [G_\sigma(i\omega = 0,\boldsymbol{\kappa})]_{26} = \int_{-\infty}^{+\infty} [G_\sigma(\tau,\boldsymbol{\kappa})]_{26} d\tau = \int_0^{+\infty} \{[G_\sigma(\tau,\boldsymbol{\kappa})]_{26} - [G_\sigma(\tau,\boldsymbol{\kappa})]^\star_{26}\} d\tau = iB_{11}$$

$$A_{12} = [G_\sigma(i\omega = 0,\mathbf{k})]_{36} = \int_{-\infty}^{+\infty} [G_\sigma(\tau,\mathbf{k})]_{36} d\tau = 2\int_0^{+\infty} [G_\sigma(\tau,\mathbf{k})]_{36} d\tau = B_{12}. \tag{E19}$$

We can observe that all the matrix elements of $G_\sigma(\tau,\boldsymbol{\kappa})$ matrix must be either purely real or purely imaginary, and the diagonal matrix elements are all zero. Hence, the matrix structure as $G_\sigma(\tau,\boldsymbol{\kappa})$ is as following,

$$G_\sigma(i\omega = 0,\boldsymbol{\kappa}) = \begin{pmatrix} 0 & B_4 & iB_5 & B_6 & iB_7 & B_8 \\ B_4 & 0 & B_9 & -iB_7 & B_{10} & iB_{11} \\ -iB_5 & B_9 & 0 & B_8 & -iB_{11} & B_{12} \\ B_6 & iB_7 & B_8 & 0 & B_4 & iB_5 \\ -iB_7 & B_{10} & iB_{11} & B_4 & 0 & B_9 \\ B_8 & -iB_{11} & B_{12} & -iB_5 & B_9 & 0 \end{pmatrix}, \tag{E20}$$

in which $\{B_i | i = 4,5,\ldots,12\}$ are purely real numbers.

APPENDIX F: TOPOLOGICAL PHASE TRANSITIONS IN THE GKMH MODEL AND CKMH MODEL

In this part, we present some more numerical data of topological invariants for across topological phase transitions for both the GKMH model in Sec. IV A and the CKMH model in Sec. IV B. For the t_d-driven topological phase transition of GKMH model in Sec. IV A, the results of both Z_2 invariant and Chern number $C_\uparrow$ (equal to spin Chern number C_s) from finite-size QMC simulations are shown in Fig. 7, at $t_3/t = 0, \lambda/t = 0.2$ and $U/t = 2.0$. The noninteracting GKMH model obtains a topological phase transition at $t_d/t = 2.0$ for $t_3/t = 0$, as long as $\lambda/t > 0$. From the results in Fig. 7, one sees the weak interaction $U/t = 2.0$ only give a small shift of the topological phase transition point. Across this t_d-driven phase transition, both the parity change and single-particle gap close happen only at the $\mathbf{M}_2$ point, due to the anisotropy [26,28,29] introduced by t_d. From the integer-quantized Z_2 invariant, the phase transition point only possesses a small shift in t_d/t, from $L = 6$ system to $L = 18$ system, in Fig. 7(a). By means of the interpolation process, with the QMC simulation results of $L = 12$ and 18, we obtain the perfect, quantized Chern number $C_\uparrow$ results in Figs. 7(b) and 7(c).

Figure 8 shows the results of Z_2 invariant $(-1)^\nu$ [Fig. 8(a)] and Chern number $C_\uparrow$ [Figs. 8(b) and 8(c)) for the case of λ_I-driven topological phase transition of CKMH model in Sec. IV B with $\alpha = 1.8, U/t = 2$, from finite-size QMC simulations of $L = 6,12$ systems and interpolation. The sharp drop of integer-valued Z_2 invariant $(-1)^\nu$ defines the topological phase transition, at $\lambda_I/t = 0.103 \sim 0.104$ for the $L = 6$ system and $\lambda_I/t = 0.100 \sim 0.101$ for the $L = 12$ system. The positions for the finite value jump of Chern number $C_\uparrow$ in $L = 6$ and $L = 12$ systems are consistent with those of Z_2 invariant $(-1)^\nu$. Across the topological phase transition, both the single-particle gap close and the parity change happen at the $\boldsymbol{\Gamma}$ point. Still, $C_\uparrow$ from QMC are not quantized integer value according to the results in Figs. 8(b) and 8(c).

The calculation results of Chern number $C_\uparrow$ after the interpolation for the λ_I-driven topological phase transition is presented in Figs. 8(b) and 8(c), from the QMC data in $L = 6$ and 12 systems. With large enough IL, the integer-valued Chern number $C_\uparrow$ can be obtained. Again, very close to the transition point, the nonmonotonic behavior of $C_\uparrow$ from interpolation method appears both in Figs. 8(b) and 8(c), when IL is not large, but it disappears after we increase IL.

[1] M. Z. Hasan and C. L. Kane, Rev. Mod. Phys. **82**, 3045 (2010).
[2] X.-L. Qi and S.-C. Zhang, Rev. Mod. Phys. **83**, 1057 (2011).
[3] K. v. Klitzing, G. Dorda, and M. Pepper, Phys. Rev. Lett. **45**, 494 (1980).

[4] F. D. M. Haldane, Phys. Rev. Lett. **61**, 2015 (1988).
[5] D. J. Thouless, M. Kohmoto, M. P. Nightingale, and M. den Nijs, Phys. Rev. Lett. **49**, 405 (1982).
[6] J. E. Avron, R. Seiler, and B. Simon, Phys. Rev. Lett. **51**, 51 (1983).
[7] C. L. Kane and E. J. Mele, Phys. Rev. Lett. **95**, 226801 (2005).
[8] C. L. Kane and E. J. Mele, Phys. Rev. Lett. **95**, 146802 (2005).
[9] L. Fu and C. L. Kane, Phys. Rev. B **74**, 195312 (2006).
[10] D. N. Sheng, Z. Y. Weng, L. Sheng, and F. D. M. Haldane, Phys. Rev. Lett. **97**, 036808 (2006).
[11] E. Prodan, Phys. Rev. B **80**, 125327 (2009).
[12] L. Fu and C. L. Kane, Phys. Rev. B **76**, 045302 (2007).
[13] H. So, Prog. Theor. Phys. **74**, 585 (1985).
[14] K. Ishikawa and T. Matsuyama, Z. Phys. C **33**, 41 (1986).
[15] G. E. Volovik, JETP **67**, 1804 (1988).
[16] Z. Wang, X.-L. Qi, and S.-C. Zhang, Phys. Rev. Lett. **105**, 256803 (2010).
[17] V. Gurarie, Phys. Rev. B **83**, 085426 (2011).
[18] G. E. Volovik, *The Universe in a Helium Droplet* (Oxford University Press New York, 2009).
[19] Q. Niu, D. J. Thouless, and Y.-S. Wu, Phys. Rev. B **31**, 3372 (1985).
[20] Z. Wang and S.-C. Zhang, Phys. Rev. X **4**, 011006 (2014).
[21] Z. Wang and S.-C. Zhang, Phys. Rev. X **2**, 031008 (2012).
[22] Z. Wang and B. Yan, J. Phys.: Condens. Matter **25**, 155601 (2013).
[23] T. Yoshida, R. Peters, S. Fujimoto, and N. Kawakami, Phys. Rev. Lett. **112**, 196404 (2014).
[24] F. Lu, J. Z. Zhao, H. Weng, Z. Fang, and X. Dai, Phys. Rev. Lett. **110**, 096401 (2013).
[25] X. Deng, K. Haule, and G. Kotliar, Phys. Rev. Lett. **111**, 176404 (2013).
[26] H.-H. Hung, L. Wang, Z.-C. Gu, and G. A. Fiete, Phys. Rev. B **87**, 121113 (2013).
[27] T. C. Lang, A. M. Essin, V. Gurarie, and S. Wessel, Phys. Rev. B **87**, 205101 (2013).
[28] H.-H. Hung, V. Chua, L. Wang, and G. A. Fiete, Phys. Rev. B **89**, 235104 (2014).
[29] Z. Y. Meng, H.-H. Hung, and T. C. Lang, Mod. Phys. Lett. B **28**, 1430001 (2014).
[30] F. Grandi, F. Manghi, O. Corradini, and C. M. Bertoni, Phys. Rev. B **91**, 115112 (2015).
[31] F. Grandi, F. Manghi, O. Corradini, C. M. Bertoni, and A. Bonini, New J. Phys. **17**, 023004 (2015).
[32] J. C. Budich, R. Thomale, G. Li, M. Laubach, and S.-C. Zhang, Phys. Rev. B **86**, 201407 (2012).
[33] J. C. Budich, B. Trauzettel, and G. Sangiovanni, Phys. Rev. B **87**, 235104 (2013).
[34] A. Amaricci, J. C. Budich, M. Capone, B. Trauzettel, and G. Sangiovanni, Phys. Rev. Lett. **114**, 185701 (2015).
[35] Y.-H. Chen, H.-H. Hung, G. Su, G. A. Fiete, and C. S. Ting, Phys. Rev. B **91**, 045122 (2015).
[36] T. Maier, M. Jarrell, T. Pruschke, and M. H. Hettler, Rev. Mod. Phys. **77**, 1027 (2005).
[37] Z. Wang, X.-L. Qi, and S.-C. Zhang, Phys. Rev. B **84**, 014527 (2011).
[38] Z. Wang, X.-L. Qi, and S.-C. Zhang, Phys. Rev. B **85**, 165126 (2012).
[39] Z. Wang and S.-C. Zhang, Phys. Rev. B **86**, 165116 (2012).
[40] F. Assaad and H. Evertz, in *Computational Many-Particle Physics*, Lecture Notes in Physics, Vol. 739, edited by H. Fehske, R. Schneider, and A. Weiße (Springer Berlin Heidelberg, 2008), pp. 277–356.
[41] H.-Q. Wu, Y.-Y. He, Y.-Z. You, C. Xu, Z. Y. Meng, and Z.-Y. Lu, Phys. Rev. B **92**, 165123 (2015).
[42] W. Wu, S. Rachel, W.-M. Liu, and K. Le Hur, Phys. Rev. B **85**, 205102 (2012).
[43] O. Parcollet, G. Biroli, and G. Kotliar, Phys. Rev. Lett. **92**, 226402 (2004).
[44] G. Biroli, O. Parcollet, and G. Kotliar, Phys. Rev. B **69**, 205108 (2004).
[45] S. Sakai, G. Sangiovanni, M. Civelli, Y. Motome, K. Held, and M. Imada, Phys. Rev. B **85**, 035102 (2012).
[46] Q.-X. Li, R.-Q. He, and Z.-Y. Lu, Phys. Rev. B **92**, 155127 (2015).